Gondwana Research xxx (2014) xxx–xxx

Contents lists available at ScienceDirect

Gondwana Research

journal homepage: www.elsevier.com/locate/gr

From continental rifting to seafloor spreading: Insight from 3D thermo-mechanical modeling

Jie Liao *, Taras Gerya

Geophysical Fluid Dynamics, Institute of Geophysics, ETH Zurich, Sonneggstrasse 5, CH-8092 Zurich, Switzerland

ARTICLE INFO

Article history:
Received 20 April 2014
Received in revised form 25 October 2014
Accepted 5 November 2014
Available online xxxx

Handling Editor: A.R.A. Aitken

Keywords:
Lithospheric coupling/decoupling
Continental rifting
Seafloor spreading
Detachment fault
3D numerical modeling

ABSTRACT

Continental rifting to seafloor spreading is a continuous process, and rifting history influences the following spreading process. However, the complete process is scarcely simulated. Using 3D thermo-mechanical coupled visco-plastic numerical models, we investigate the complete extension process and the inheritance of continental rifting in oceanic spreading. Our modeling results show that the initial continental lithosphere rheological coupling/decoupling at the Moho affects oceanic spreading in two manners: (1) coupled model (a strong lower crust mechanically couples upper crust and upper mantle lithosphere) generates large lithospheric shear zones and fast rifting, which promotes symmetric oceanic accretion (i.e. oceanic crust growth) and leads to a relatively straight oceanic ridge, while (2) decoupled model (a weak ductile lower crust mechanically decouples upper crust and upper mantle lithosphere) generates separate crustal and mantle shear zones and favors asymmetric oceanic accretion involving development of active detachment faults with 3D features. Complex ridge geometries (e.g. overlapping ridge segments and curved ridges) are generated in the decoupled models. Two types of detachment faults termed continental and oceanic detachment faults are established in the coupled and decoupled models, respectively. Continental detachment faults are generated through rotation of high angle normal faults during rifting, and terminated by magmatism during continental breakup. Oceanic detachment faults form in oceanic crust in the late rifting–early spreading stage, and dominates asymmetric oceanic accretion. The life cycle of oceanic detachment faults has been revealed in this study.

1. Introduction

The continuous process from continental rifting to seafloor spreading is a key step in Wilson's cycle (Wilson, 1966), but the complete process is scarcely simulated. Understanding the inheritance of continental rifting in seafloor spreading is crucial to study the incipient oceanic ridge evolution and remains a big challenge (Lister et al., 1986; Taylor et al., 1999; Ebinger and Casey, 2001; Nielsen and Hopper, 2004; Taylor et al., 2009; Gerya, 2012). Compared to the continental rifting process, which has been widely studied by numerical and analogue modeling (Buck, 1991; Buck et al., 1999; Huismans and Beaumont, 2003; Corti, 2008, 2012), few studies have been done on the complete rifting–spreading process due to several difficulties. One difficulty is that the long extension process requires large strain to reach the final steady state of seafloor spreading from the initial intact continental lithosphere, and it includes many complex geodynamic processes, such as partial melting of the asthenospheric mantle, melt extraction and percolation towards surface, magmatic accretion of new oceanic crust and hydrothermal circulation at the axis of ridges resulting in excess cooling of oceanic crust (Gerya, 2010, 2013). Another difficulty is that oceanic spreading is by its nature a 3D problem, as large heterogeneities are present along oceanic ridges. Ultra-slow spreading ridges are mostly oblique to spreading directions and consist of alternating magmatic–amagmatic segments (Dick et al., 2003). Symmetric and asymmetric oceanic accretion (i.e. oceanic crust growth) are alternatively distributed along slow spreading ridges (Escartin et al., 2008). Overlapping spreading centers and transform faults are two common ways that oceanic segments interact ((Gerya, 2012), and references therein). These 3D features of oceanic ridges naturally require 3D models. Furthermore, the deficit of direct natural observations makes the rifting–spreading transition enigmatic. Unlike the widely distributed examples of continental rifts and oceanic ridges, very few natural examples record the rifting–spreading transition, and some good examples are the Woodlark Basin in the southwestern Pacific ocean (Taylor et al., 1999, 2009), the Laptev Sea margin in the Arctic ocean (Franke et al., 2001; Engen et al., 2003) and the Red Sea-Gulf of Aden system (d'Acremont et al., 2010; Leroy et al., 2010; Ligi et al., 2012; Brune and Autin, 2013).

As commonly believed (Dunbar and Sawyer, 1988, and references therein), continental rifts do not occur randomly, but tend to follow pre-existing weaknesses (such as fault zones, suture zones, failed rifts, and other tectonic boundaries) in the lithosphere, although explanations for the earliest weaknesses formed in the proto-lithosphere are debated. Many natural examples prove that the way rifts develop is to

* Corresponding author.
E-mail address: jie.liao@erdw.ethz.ch (J. Liao).

http://dx.doi.org/10.1016/j.gr.2014.11.004
1342-937X/

follow pre-existing lithospheric structures, for instance, the western branch of East African Rift (Nyblade and Brazier, 2002; Corti et al., 2007), the Main Ethiopian Rift (Corti, 2009), and the Baikal rift (Petit and Deverchere, 2006). The early-stage formed rift can be a template for the future rift development and continental breakup. However, numerous heterogeneities are generated during continental rifting, and rift propagation may divert from the initial rift trend (i.e. trend of pre-existing weakness), just as it has been proposed for the Main Ethiopian Rift (Keranen and Klemperer, 2008; Corti, 2009). To what extent rifting history influences continental breakup and seafloor spreading is hardly constrained. Moreover, the influence of rifting history on continental breakup and seafloor spreading is related to the formation of transform faults. One possible mechanism of transform fault formation which is widely proposed is related to the inheritance of pre-existing lithospheric weaknesses. Transform faults may initiate and develop along pre-existing zones of weakness that are nearly perpendicular to oceanic ridges, such as the long transform fault in the equatorial Atlantic ridge between South America and Africa (Wilson, 1965). The correspondence between the passive margins and the transform faults in the Gulf of Aden also suggests the possibility of inheritance of pre-existing weakness in some transform fault formation (d'Acremont et al., 2010).

Symmetric and asymmetric accretion are two oceanic ridge spreading modes. Symmetric oceanic accretion is featured by the roughly symmetrically distributed abyssal hills on both flanks of an oceanic ridge, while asymmetric oceanic accretion is characterized by the development of active detachment faults along one flank, and most of the detachment faults have 3D curved (convex towards ridge) geometries on a map view (Buck et al., 2005; Smith et al., 2006; Escartin et al., 2008). On a gross scale, oceanic accretion pattern has a strong relation with spreading rates. Asymmetric accretion is favored by slow spreading, while symmetric accretion is promoted by fast spreading (Buck et al., 2005; Puthe and Gerya, 2014, and references therein). On a small scale, however, alternating segments of symmetric and asymmetric oceanic accretion are observed along slow spreading ridges where the spreading rate varies slightly, such as the northern Mid-Atlantic Ridge (Escartin et al., 2008). In this case, the alternating symmetric/asymmetric oceanic accretion pattern is difficult to explain by variations in the spreading rate alone.

Allken et al. (2011) and Allken and Huismans (2012) investigated continental rift propagation and interaction in the upper crust through 3D numerical modeling using relatively simple temperature-independent (visco)-plastic rheologies. Extension strain in these studies was insufficient to reach continental breakup. Oblique extension of continental rifting is investigated based on 3D numerical modeling (Brune et al., 2012; Brune and Autin, 2013; Brune, 2014). Although continental breakup was reached in these models, seafloor spreading (e.g. oceanic crust accretion) was not simulated. Gerya (2010), Gerya (2013) and Puthe and Gerya (2014) numerically modeled the transform fault initiation (and development) and ridge segment interaction in 3D based on an incipient oceanic ridge or an idealized thinned continental lithosphere. Besides, several other 3D numerical modelings have been conducted with focuses on different stages of the rifting–spreading process (Van Wijk, 2005; Van Wijk and Blackman, 2005; Choi et al., 2008; Gregg et al., 2009), but the complete process is scarcely simulated.

In this study, we aim to investigate inheritance of continental rifting on incipient seafloor spreading by modeling the complete rifting–spreading process, with particular attention paid on the two oceanic accretion modes (symmetric and asymmetric accretion). The initial rheological structure of continental lithosphere and the geometry of a pre-existing weak zone are the two key parameters that we study. Two rheological structures named decoupled (DCP) and coupled (CP) are distinguished by the presence/absence of a strong lower crustal layer. Two types of model setup in terms of the weak zone geometry are investigated, one is 2D-like setup (i.e. a long planar extension-orthogonal weak zone going through the entire model box) and the other is 3D-like setup (i.e. a short weak zone going through part of the model box). The influence of the weak zone location (i.e. in upper crust or in uppermost lithospheric mantle) has also been investigated. Our preliminary modeling results show that the asymmetric oceanic accretion involved with active detachments is favored by DCP models, while CP models typically generate symmetric oceanic accretion. Initiation, development and termination of detachment faults, curved geometry of oceanic detachment faults, inheritance of continental rifting on seafloor spreading, and magmatism along passive margins are discussed.

2. Numerical implementation and model setup

2.1. Governing equations

The 3D thermo-mechanical coupled numerical code (Gerya, 2013) based on conservative finite-differences and marker-in-cell techniques is used to solve the mass, momentum and energy conservation equations for incompressible media:

$$\frac{\partial v_i}{\partial x_i} = 0 \tag{1}$$

$$\frac{\partial \sigma_{ij}}{\partial x_j} - \frac{\partial P_i}{\partial x_i} = -\rho g_i \tag{2}$$

$$\rho C_{p,eff} \frac{DT}{Dt} = \frac{\partial}{\partial x_i}\left(k \frac{\partial T}{\partial x_i}\right) + H_r + H_s + H_a \tag{3}$$

where v is velocity, σ the deviatoric stress tensor, P the total pressure (mean normal stress), ρ the density, g the gravitational acceleration, $C_{p,eff}$ the effective heat capacity (explained in below), T the temperature, k the thermal conductivity, H_r the radioactive heating, $H_s = \sigma\,\dot{\epsilon}$ the shear heating (product of deviatoric stress and strain rate), and $H_a = T\alpha\frac{DP}{Dt}$ the adiabatic heating. The Einstein notation is used for the indexes i and j, which denote spatial directions i = (x, y, z) and j = (x, y, z) in 3D. Lagrangian temperature equation is solved on the Eulerian nodes, and temperature increments are interpolated from nodes to markers by using the subgrid diffusion operation (Gerya and Yuen, 2003, 2007; Gerya, 2010), which can ensure physical consistence between nodal and marker thermal fields. Advection of temperature is implemented through marker advection. The Multigrid method is used to speed up the convergence of the Gauss-Seidel iterations for coupled solving of mass and momentum conservation equations. OpenMp-based parallelization is used in computation.

2.2. Rock rheology implementation

Visco-plastic rheology is implemented in our numerical models and Drucker-Prager yield criterion is used to determine whether viscous deformation or plastic deformation occurs. Viscous creep dominates model deformation when second invariant of deviatoric stress $\left(\sigma_{II} = \left(\frac{1}{2}\sigma_{ij}\sigma_{ij}\right)^{\frac{1}{2}}\right)$ is less than the plastic yielding criterion (σ_y). Effective creep viscosity which represents the competition between diffusion and dislocation creeps (Ranalli, 1995) is expressed as: $\eta = 1/(1/\eta_{diff} + 1/\eta_{disl})$, where η_{diff} and η_{disl} are computed as:

$$\eta_{diff} = \frac{1}{2} A_d {\sigma_{crit}}^{1-n} \exp\left(\frac{PV_a + E_a}{RT}\right) \tag{4}$$

$$\eta_{disl} = \frac{1}{2} A_d^{1/n} \dot{\epsilon}_{II}^{(1-n)/n} \exp\left(\frac{PV_a + E_a}{nRT}\right) \tag{5}$$

Please cite this article as: Liao, J., Gerya, T., From continental rifting to seafloor spreading: Insight from 3D thermo-mechanical modeling, Gondwana Research (2014), http://dx.doi.org/10.1016/j.gr.2014.11.004

where A_d is the pre-exponential constant, n is the stress/strain rate exponent, V_a is the activation volume, E_a is the activation energy, R is the gas constant (8.314 J/K/mol), $\sigma_{crit} = 10^4$ Pa is the transition stress from diffusion to dislocation creep (Turcotte and Schubert, 2002), and $\dot{\epsilon}_{II}$ is the second invariant of strain rate ($\dot{\epsilon}_{II} = \left(\frac{1}{2}\dot{\epsilon}_{ij}\dot{\epsilon}_{ij}\right)^{\frac{1}{2}}$). Diffusion creep is implemented in a simplified way: (1) grain size is assumed to be constant and (2) transition from diffusion to dislocation creep is assumed to occur at the constant critical stress irrespective of temperature and pressure. Since deviatoric stress magnitude inside our models is significantly higher than 10^4 Pa, diffusion creep is always playing very minor role during viscous deformation, and this is rather typical for the continental lithosphere, where dislocation creep is regarded as the dominant mechanism (Karato, 1992, 2010). Once the yielding criterion $\sigma_{II} >= \sigma_y$ is reached, effective viscosity is computed as:

$$\eta = \frac{\sigma_y}{2\dot{\epsilon}_{II}} = \frac{C_o + \left(P - P_f\right)\phi}{2\dot{\epsilon}_{II}} \tag{6}$$

where C_o is the cohesion (i.e. residual strength of rock when pressure is zero), ϕ is the coefficient of internal friction, P_f is the hydrostatic fluid pressure, $\dot{\epsilon}_{II}$ is the second invariant of strain rate. Plastic strain weakening is implemented by linearly decreasing the cohesion (from C_o^0 to C_o^1) and the coefficient of internal friction (from ϕ^0 to ϕ^1) between the strain interval 0.25–1.25. A constant plastic healing rate (10^{-13} s^{-1}, comparable to the plastic strain rate inside active faults) is applied to heal the deactivated fractures (Gerya, 2013). At sufficient high stress ($\sigma_{II} > 200$ MPa) and low temperature ($T < 1100$ °C), Peierls creep takes over from dislocation creep. In our model, the Peierls creep is implemented similarly to the plasticity i.e. equilibrium σ_{II} is computed for a given $\dot{\epsilon}_{II}$ using Eq. (7) (Katayama and Karato, 2008) by bisection:

$$\dot{\epsilon}_{II} = A_{Pei}\sigma_{II}^2 \exp\left\{-\frac{PV_a + E_a}{RT}\left[1 - \left(\frac{\sigma_{II}}{\sigma_{Pei}}\right)^m\right]^{n_{Pei}}\right\} \tag{7}$$

where $\sigma_{Pei} = 9.1 \times 10^9$ Pa, $A_{Pei} = 6.3 \times 10^{-5}$ Pa^{-2} s^{-1}, $m = 1$, $n_{Pei} = 2$ are experimentally determined parameters (Katayama and Karato, 2008). Effective viscosity is thus limited by $\eta = \sigma_{II}/2\dot{\epsilon}_{II}$.

2.3. Magma-related processes implementation

Magma-related processes (i.e. melt generation, extraction, percolation and accretion) are implemented in our models in a simplified way (Gerya, 2013). The melt fraction (M) of the dry mantle is calculated based on the parameterized melting model from Katz et al. (2003):

$$M = \left(\frac{T - T_{solidus}}{T_{liquidus}^{lherz} - T_{solidus}}\right)^{n_{cpx}}, \text{when } T_{solidus} < T < T_{cpx-out} \tag{8}$$

$$M = M_{cpx-out} + \left(1 - M_{cpx-out}\right)\left(\frac{T - T_{cpx-out}}{T_{liquidus} - T_{cpx-out}}\right)^{n_{opx}}, \text{when } T_{cpx-out} < T < T_{liquidus} \tag{9}$$

where $T_{solidus}$, $T_{liquidus}$ and $T_{liquidus}^{lherz}$ are the mantle solidus, mantle liquidus, and lherzolite liquidus, respectively. $n_{cpx} = n_{opx} = 1.5$ are the exponents. $M_{cpx\ -\ out} = 0.15/(0.5 + 8 \times 10^{-5}P)$ (P in unit of MPa) and $T_{cpx-\mathrm{out}} = M_{cpx-\mathrm{out}}^{n_{cpx}^{-1}}\left(T_{\mathrm{liquidus}}^{\mathrm{lherz}} - T_{\mathrm{solidus}}\right) + T_{\mathrm{solidus}}$ are the melt fraction and temperature when cpx is exhausted through melting, respectively. Eq. (9) means that clinopyroxene (cpx) is exhausted in the mantle, and melting consumes mostly orthopyroxene (opx).

Partial melting occurs in a wide area similar to the melt pooling region proposed by Gregg et al. (2009), and melt is extracted and stored in the shallowest part of the partial melting area. Lagrangian markers track the amount of melt extracted during model evolution. At each time step, a certain amount of melt is extracted based on the following formulation:

$$\delta M = M - \sum_{i=1}^{n} M_i^{ext} \tag{10}$$

where n represents the previous extraction episodes, M_i^{ext} the extracted melt at each time step. The rock is considered non-molten when extracted melt fraction is larger than the standard melt fraction ($\delta M < 0$). Extracted melt is instantaneously transported to the shallowest part of the melting pool and forms a magma chamber. This means that melt transportation is not modeled explicitly, but implemented by converting the rock type in the shallowest part of the melting pool to a new rock type (i.e. molten mantle to molten basalt). The total volume of the converted markers matches the total volume of extracted melt at each time step. Extracted melt at the next time step will be added to the bottom of the magma chamber. If basalt solidifies locally in the magma chamber, oceanic crust generation (magmatic accretion) occurs spontaneously at the walls of the magma chamber, by simply converting the rock type from molten to solid basalt (cf. Gerya (2013) for crust crystallization algorithm details). This simple crust accretion algorithm does not account for volcanic and diking processes (Buck et al., 2005; Wanless and Shaw, 2012) above the magma regions, neither does it account for internal convection, melt segregation and crystal differentiation inside these regions (Wanless and Shaw, 2012).

Effective values of the physical parameters of the partially molten mantle (density, heat capacity, heat conductivity, thermal expansion, and compressibility) are modified based on melt fraction (Eq. (11)). Latent heating effect due to melting/crystallization equilibrium is included implicitly by further increasing the effective heat capacity and thermal expansion in the energy conservation equation:

$$X_{eff} = X_{molten} \times M + X_{solid} \times (1 - M) \tag{11}$$

$$C_{p,eff} = C_p + Q_L\left(\frac{\partial M}{\partial T}\right)_p \tag{12}$$

$$\alpha_{eff} = \alpha + \rho\frac{Q_L}{T}\left(\frac{\partial M}{\partial P}\right)_T \tag{13}$$

where X_{eff} represents the effective value of a physical parameter, X_{solid} and X_{liquid} are the values in solid and liquid states, respectively, and Q_L the latent heat. Material parameters are shown in Tables 1 and 2.

2.4. Model setup

The numerical model box used in this study is cubic (Fig. 1a) with a high resolution of 197 × 197 × 197 regular distributed nodes (corresponding to dimensions of 98 × 98 × 98 km) and around 60 million randomly distributed Lagrangian markers. A 5 km-thick sticky air layer ($\rho = 1$ kg/m^3, $\eta = 10^{18}$ Pa s, $k = 200$ W/m/K) is imposed in the uppermost part of the model box, which approximates the upper surface of the crust as a free surface (Schmeling et al., 2008; Crameri et al., 2012). The crustal and mantle layers are located below. During model development and the related crustal surface deformation, transmutation of sticky air markers into sticky water ($\rho = 1000$ kg/m^3, $\eta = 10^{18}$ Pa s, $k = 200$ W/m/K) occurs when these markers move below the prescribed water level (0.5 km below initial crustal surface). Further transmutation of water markers into sediments occurs below the prescribed sedimentation level (10 km below initial crustal surface). Instantaneous erosion is prescribed at 4 km above the initial crustal level by converting rock markers into sticky air.

Two different lithospheric rheological coupling structures in terms of the absence/presence of a strong lower crust are used in our models,

Please cite this article as: Liao, J., Gerya, T., From continental rifting to seafloor spreading: Insight from 3D thermo-mechanical modeling, Gondwana Research (2014), http://dx.doi.org/10.1016/j.gr.2014.11.004

Table 1
Material parameters used in the numerical experiments.[a]

	(Upper) crust[b]	Lower crust	Mantle	Crustal weak zone	Mantle weak zone	Reference[c]
Flow law	Wet quartzite	Plagioclase	Dry olivine	Wet quartzite	Wet olivine	
ρ (kg m^{-3})	2750	3000	3300	2700	3200	1
C_o^0 (Pa)	1×10^7	1×10^7	1×10^7	3×10^6	3×10^6	2
C_o^1 (Pa)	3×10^6	3×10^6	3×10^6	3×10^6	3×10^6	
ϕ_{DCP}^0	0.258	0.6	0.6	0.1	0.0	2
ϕ_{DCP}^1	0.035	0.0	0.0	0.035	0.0	
ϕ_{CP}^0	0.4	0.4	0.64	0.2	0.2	2
ϕ_{CP}^1	0.12	0.12	0.12	0.06	0.06	
E_a (J mol^{-1})	1.54×10^5	2.38×10^5	5.32×10^5	1.54×10^5	4.7×10^5	2
V_a (m^3 mol^{-1})	0	0	1.6×10^{-5}	0	1.6	2
A_D (Pa^n s)	1.97×10^{19}	4.8×10^{22}	3.98×10^{16}	1.97×10^{19}	5.01×10^{20}	2
n	2.3	3.2	3.5	2.3	4	2
H_r (μW m^{-3})	2.0	0.25	0.022	1.0	0.022	1
Q_L (kJ kg^{-1})	300	400	400	380	400	1, 3

[a] : See the text for the explanations of the symbols. Other parameters (for all rocks): $C_p = 1000$ J kg^{-1} K^{-1}, $\alpha = 3 \times 10^{-5}$ K^{-1}, $\beta = 1 \times 10^{-5}$ MPa^{-1}.
[b] : Represents upper crust in the coupled rheology (CP), and entire crust in the decoupled rheology (DCP).
[c] : 1 — (Turcotte and Schubert, 2002), 2 — (Ranalli, 1995), and 3 — (Bittner and Schmeling, 1995).

named decoupled rheology (DCP, i.e. with a weak lower crust) and coupled rheology (CP, i.e. with strong lower crust) (Fig. 1b). The initial strength envelope (computed by assuming a constant strain rate), to a first order, represents the lithospheric strength (Afonso and Ranalli, 2004; Burov and Watts, 2006; Burgmann and Dresen, 2008). Depending on composition, geotherm, and crustal/mantle thickness, the initial strength envelope varies largely from one area to another (Maggi et al., 2000; Jackson, 2002; Afonso and Ranalli, 2004; Burov and Watts, 2006; Burov, 2010). Except the rheology of the upper crust, which is commonly described by wet quartzite, rheologies of the lower crust (can be more felsic or mafic, dry or wet) and the mantle (can be described by dry or wet olivine) have been relatively less constrained, which indicates that there is a large range of available rheological structures that we can employ in our model. Here, we employ a weak felsic crust (described by wet quartzite) and a strong lithospheric mantle for the decoupled rheology. Although the crust is a uniform layer, the lower part behaves in a ductile way (left panel in Fig. 1b). For the coupled rheology, a strong mafic lower crust (with a thickness of 12.5 km) described by plagioclase rather than quartzite-dominated rheology is imposed to mechanically couple the upper crust and the uppermost mantle (right panel in Fig. 1b). The lithospheric mantle layer is uniform and described by dry olivine. The major plastic parameter i.e. the coefficient of internal friction (ϕ) used in the decoupled rheology differs from that in the coupled rheology. The typical value of ϕ for dry fractured crystalline rocks varies from 0.6 (when $P > 200$ MPa) to 0.85 (when $P < 200$ MPa) (Byerlee, 1978). However, if fluids are involved, the value of ϕ can dramatically decrease. The effective ϕ varies greatly depending on pore pressure which is largely unconstrained (Brace and Kohlstedt, 1980; Buck, 2006). In order to sufficiently decouple upper crust and upper mantle, relatively low ($\phi = 0.258$) and high ($\phi = 0.6$) values are used for the crust and mantle, respectively. A moderate value ($\phi = 0.4$) is taken for both the crust and mantle in the coupled rheology. Rock properties are listed in Table 1.

Two different idealized model setups in terms of the geometry of the weak zone are employed, named 2D-like and 3D-like setups (Fig. 1c and d). The 2D-like setup means that a long planar extension-orthogonal weak zone extends throughout the model box along the direction perpendicular to extension (z-direction, Fig. 1c), while the 3D-like setup (Fig. 1d) consists of a short weak zone which only has one quarter of the length of the weak zone in the 2D-like setup. Different positions of the weakness (i.e. either at the side or at the middle of the model along z-direction) are also investigated in the models with the 3D-like setup (Fig. 1d). Lithospheric weakness can either reduce crustal strength or mantle strength, and leads to a crustal or mantle dominated thinning (Dunbar and Sawyer, 1988), which completes continental breakup. In our models, the weak zone is imposed either in the upper crust or in the uppermost mantle. Lower crustal weak zones, which may also influence lithospheric deformation (Sokoutis et al., 2007), are beyond the scope of this paper.

Constant time-independent extension velocity (half rate 1.5 cm/yr) is prescribed uniformly along the entire left and right model boundaries (Fig. 1). Compensating velocities on the upper and lower boundaries are

Table 2
Pressure-and temperature-dependent parameters.

	$T_{solidus}$ (K)	Ref.[b]
Crust	$889 + 536.6/(0.03P + 1.609) + 18.21/(0.03P + 1.609)^2$ at $P < 1200$ MPa, $831.3 + 0.06P$ at $P \geq 1200$ MPa	1, 2
Mantle	$1358.85 + 0.1329P - 5.104 \times 10^{-6}P^2$	3
Hydrated mantle	$1239.8 + 1493.0/(0.03P + 9.701)$ at $P < 2400$ MPa, $1266.3 - 0.011844P + 3.5 \times 10^{-6}P^2$ at $P \geq 2400$ MPa	4
	$T_{liquidus}$ (K)	
Crust	$1262.0 + 0.09P$[a]	1
Mantle	$2053.15 + 0.045P - 2 \times 10^{-6}P^2$ ($T_{liquidus}$)	
	$1748.15 + 0.080P - 3.2 \times 10^{-6}P^2$ ($T_{liquidus}^{lher}$)	3
Hydrated mantle	$2073.15 + 0.114P$	5
	k (W m^{-1} K^{-1})	
Crust	$[1.18 + 474/(T + 77)]\exp(0.00004P)$	6
Mantle	$[0.73 + 1293/(T + 77)]\exp(0.00004P)$	6
Weak zone	$[0.73 + 1293/(T + 77)]\exp(0.00004P)$	6

[a] : Pressure in unit of MPa.
[b] : 1 — (Johannes, 1985), 2 — (Poli and Schmidt, 2002), 3 — (Katz et al., 2003) 4 — (Schmidt and Poli, 1998), 5 — (Hess, 1989), and 6 — (Clauser and Huenges, 1995).

Please cite this article as: Liao, J., Gerya, T., From continental rifting to seafloor spreading: Insight from 3D thermo-mechanical modeling, Gondwana Research (2014), http://dx.doi.org/10.1016/j.gr.2014.11.004

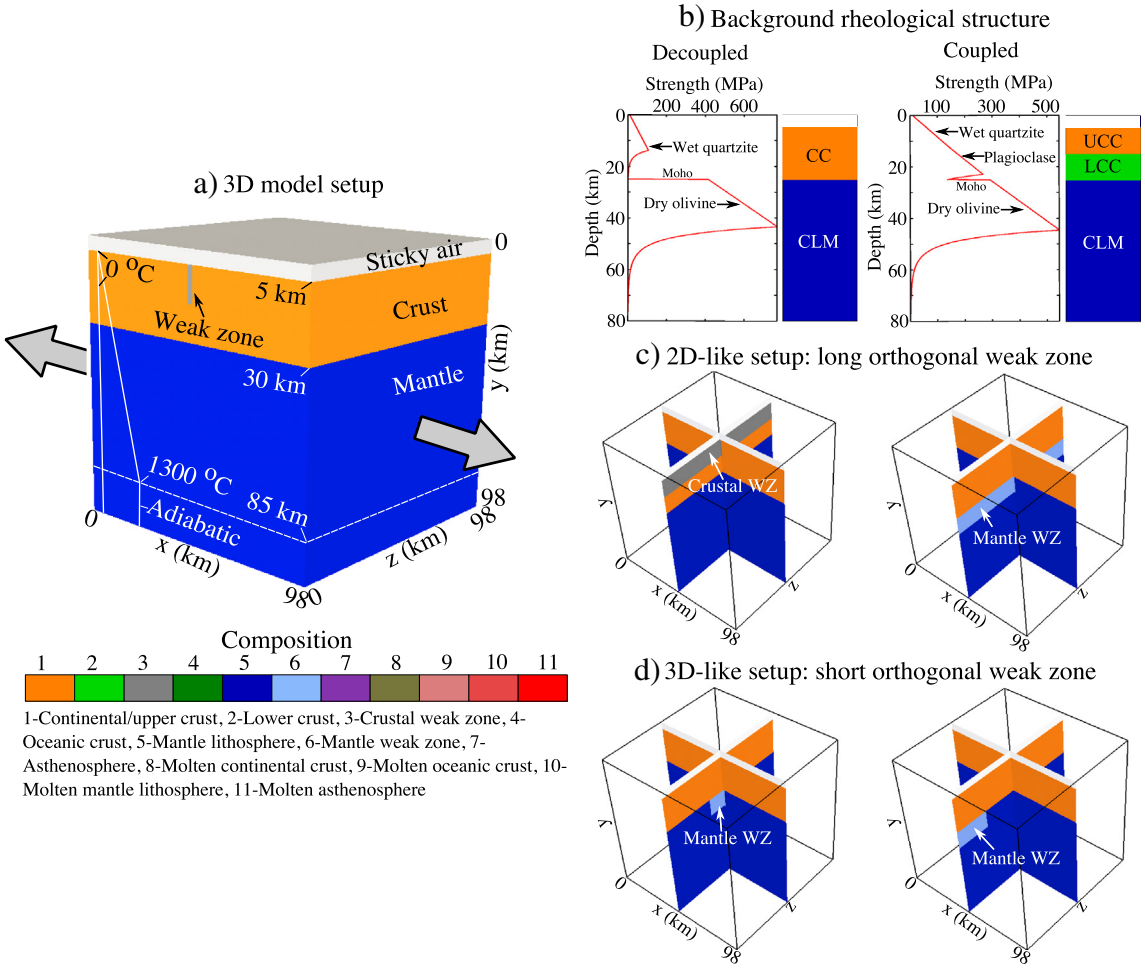

Fig. 1. Initial model configuration. (a) An example setup of a 3D model (corresponds to the decoupled rheology with a 2D-like weak zone). Arrows show boundary extension velocities (on the entire surface, and the half extension rate is 1.5 cm/yr). A sticky air layer is prescribed to approximate the crustal surface as a free surface. (b) Two different rheological structures of the lithosphere named decoupled and coupled rheology. The coupled rheology is implemented by imposing a strong lower crust. CC — continental crust, CLM — continental lithospheric mantle, UCC — upper continental crust, LCC — lower continental crust, WZ — weak zone. (c) 2D-like model setups shown by 3D slices. Crustal weak zone (left panel) or mantle weak zone (right panel) is perpendicular to extension, and goes through the entire model box (with dimensions of $2 \times 12.5 \times 98$ km). (d) 3D-like model setups. The weak zone does not go through the entire model box (with dimensions of $2 \times 12.5 \times 24.5$ km).

calculated on the basis of mass conservation for the sticky air and crustal–mantle layers, respectively (Liao and Gerya, 2014). Front and back boundaries are free slip. Initial temperature of the lithosphere is horizontally uniform and increases linearly along vertical direction from 0 °C on the surface to 1300 °C at the depth of 85 km (bottom of lithosphere), below which mantle has adiabatic temperature gradient of 0.5 °C/km. A constant temperature condition is used for the upper (0 °C) and lower boundaries (1306.5 °C). The thermal insulating boundary condition (i.e. zero conductive heat flux) is used for all side boundaries.

3. Model results

We investigate the effect of rheological coupling/decoupling, weak zone geometry, and weak zone location on continental rifting and seafloor spreading. Subsection 3.1 shows the modeling results using the 2D-like setups (i.e. long weak zone), while models in Subsection 3.2 employ the 3D-like (i.e. short weak zone) model setups. In each section, models with different rheological structures (coupling or decoupling) and weak zone locations (in the upper crust or in the uppermost lithospheric mantle) are compared. For better visualization, the sticky air and water overlying the crust (or exhumed mantle) have been removed in the 3D snapshots, and the interfaces between different layers are drawn with dashed lines.

3.1. 2D-like model setup

3.1.1. Decoupled rheology (DCP)

Dynamic evolution (shown by effective viscosity) of the models with decoupled rheology is compared in Fig. 2 and Fig. 4. A long narrow weak zone with an orientation perpendicular to the extension direction is implemented either in the upper crust (Figs. 2a–d) or in the uppermost mantle (Figs. 2e–h). Since the weak zone reduces the brittle strength of the upper crust/mantle, strain localizes rapidly. In Model 1, crustal thinning is dominant in the early stage and generates an early rift valley. Mantle extension becomes dominant after a short extension time, and breaks up the lithosphere. An interesting phenomenon is that mantle thinning concentrates in a new location which is offset laterally with the crustal thinning center. As a consequence, the final spreading ridge, that inherits the zone of mantle thinning, is offset from the early crustal rift valley which becomes abandoned. Although the 2D-like setup is used in this model, 3D features of model deformation are observed, for instance, the intensity of magmatism varies along the direction perpendicular to extension (Fig. 2d).

Please cite this article as: Liao, J., Gerya, T., From continental rifting to seafloor spreading: Insight from 3D thermo-mechanical modeling, Gondwana Research (2014), http://dx.doi.org/10.1016/j.gr.2014.11.004

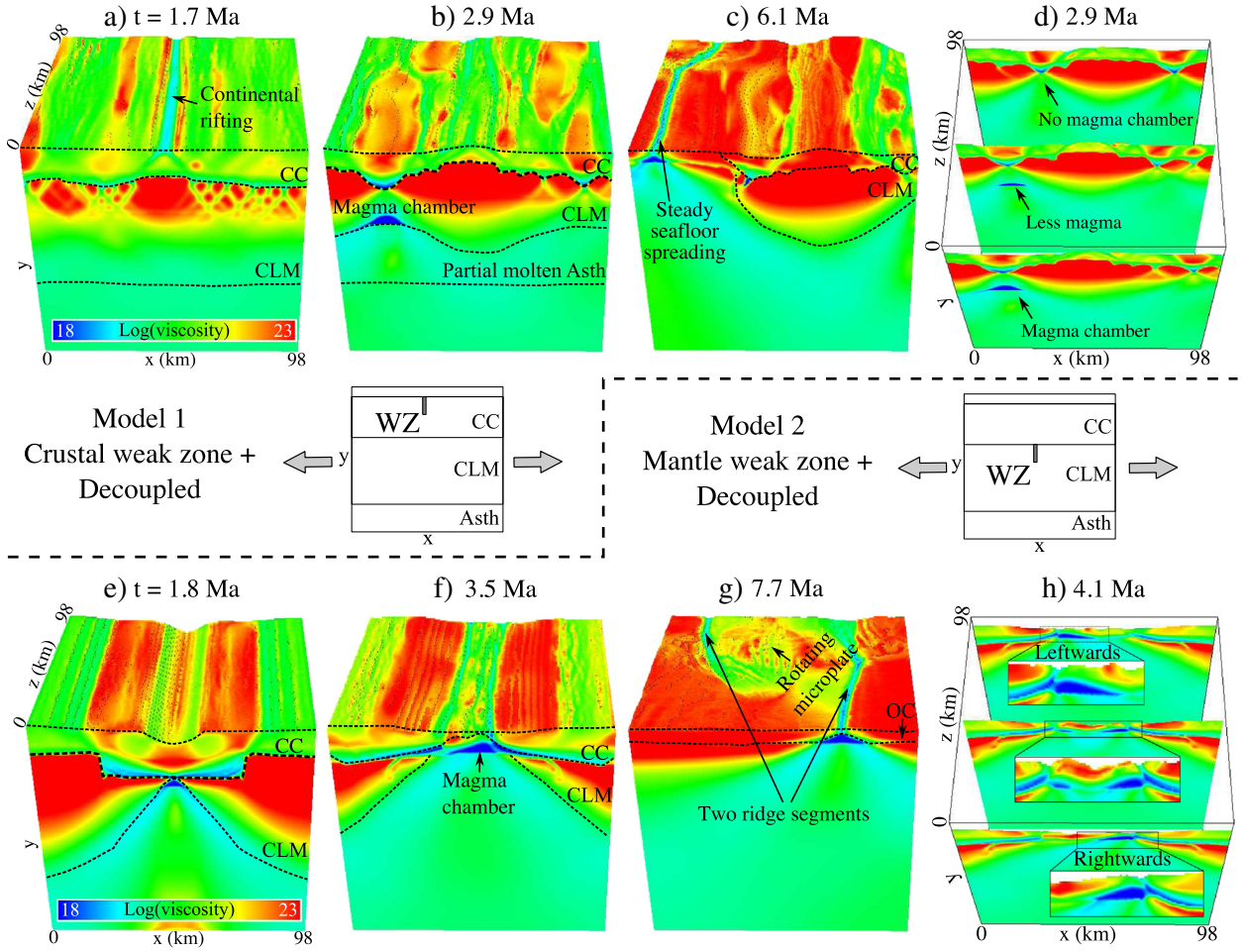

Fig. 2. Dynamic evolution of models with the lithospheric decoupled rheology shown by effective viscosity. The 2D-like setups with crustal weak zone (a–d) and mantle weak zone (e–h) are investigated (also see Fig. 1c for weak zone location). 2D slices (d and h) show the variations of model deformation along z-direction (perpendicular to extension). Note that although the model setups are 2D like, 3D features of deformation have been observed in both models. WZ — weak zone, CC — continental crust, CLM — continental lithospheric mantle, and Asth — asthenosphere. Dashed lines show the interfaces between different rock layers.

In Model 2, where a weak zone locates in the upper lithospheric mantle, distinct model evolution is observed (Model 2, Fig. 2e–h). Lithospheric mantle thinning following the pre-existing weak zone dominates lithospheric deformation from the beginning. The straight continental rift that forms above the weak zone in the early extension stage, gradually develops into two overlapping oceanic ridges. A rotating micro-plate develops between these two ridges. Formation of the overlapping ridges is related to the formation of two detachment faults which orient in opposite directions along the rift strike (Fig. 2f and h). Detachment faults result in asymmetric plate accretion, and the offset distance between the two opposite-orientated oceanic detachment faults increases with extension, which leads to two separate oceanic ridges (Fig. 4b). Transform faults are not established in this model.

3.1.2. Coupled rheology (CP)

In the coupled rheology models, a strong lower crust (with a thickness of 12.5 km) is used to mechanically couple the upper crust and the uppermost lithospheric mantle. Model 3 (with a crustal weak zone) and Model 4 (with a mantle weak zone) generate similar extension patterns: a roughly straight oceanic ridge develops from a straight continental rift. The symmetric lithospheric conjugate shear zones that are formed in the early extension stage (Fig. 3a and e) become asymmetric due to plastic strain weakening and shear heating (Fig. 3b, f). One branch of the conjugate faults becomes dominant, and is further rotated by the upwelling mantle to a low angle continental detachment fault. A small amount of mantle rock is exhumed along the ocean–continent transition zones. In a relatively short time period, both models reach steady state of seafloor spreading, and the oceanic ridges are featured by symmetric accretion (Figs. 3c, g, 4c and d). Oceanic detachments are not generated in the CP models. Slight variation is present along the rift/ridge strike (perpendicular to extension) (Fig. 3d and h).

3.1.3. Model comparison

The DCP models generate numerous heterogeneities along continental rift strike, which lead to significant 3D features (Fig. 4a and b). Deformation is more distributed in DCP models compared to the CP models (for instance the widespread molten asthenosphere), and longer extension time is required for the models to reach the steady state of seafloor spreading. Breakup of the lithospheric mantle occurs earlier than that of the crust in DCP models, indicating depth-dependent extension (Huismans and Beaumont, 2011). Large magma chambers are generated in the DCP models (Fig. 4e), such as in Model 1, which may be caused by the fast lithospheric mantle thinning and wide asthenosphere upwelling (e.g. widespread molten asthenosphere in Fig. 4b). Growth rate of the oceanic crust becomes constant once the seafloor spreading reaches the steady state (Fig. 4f). Since the (full) seafloor spreading rate equals the (full) extension rate on the side boundaries (3 cm/yr), the steady growth rate of ~100 km^3/Ma/km (growth rate per km of ridge length) indicates an

Please cite this article as: Liao, J., Gerya, T., From continental rifting to seafloor spreading: Insight from 3D thermo-mechanical modeling, Gondwana Research (2014), http://dx.doi.org/10.1016/j.gr.2014.11.004

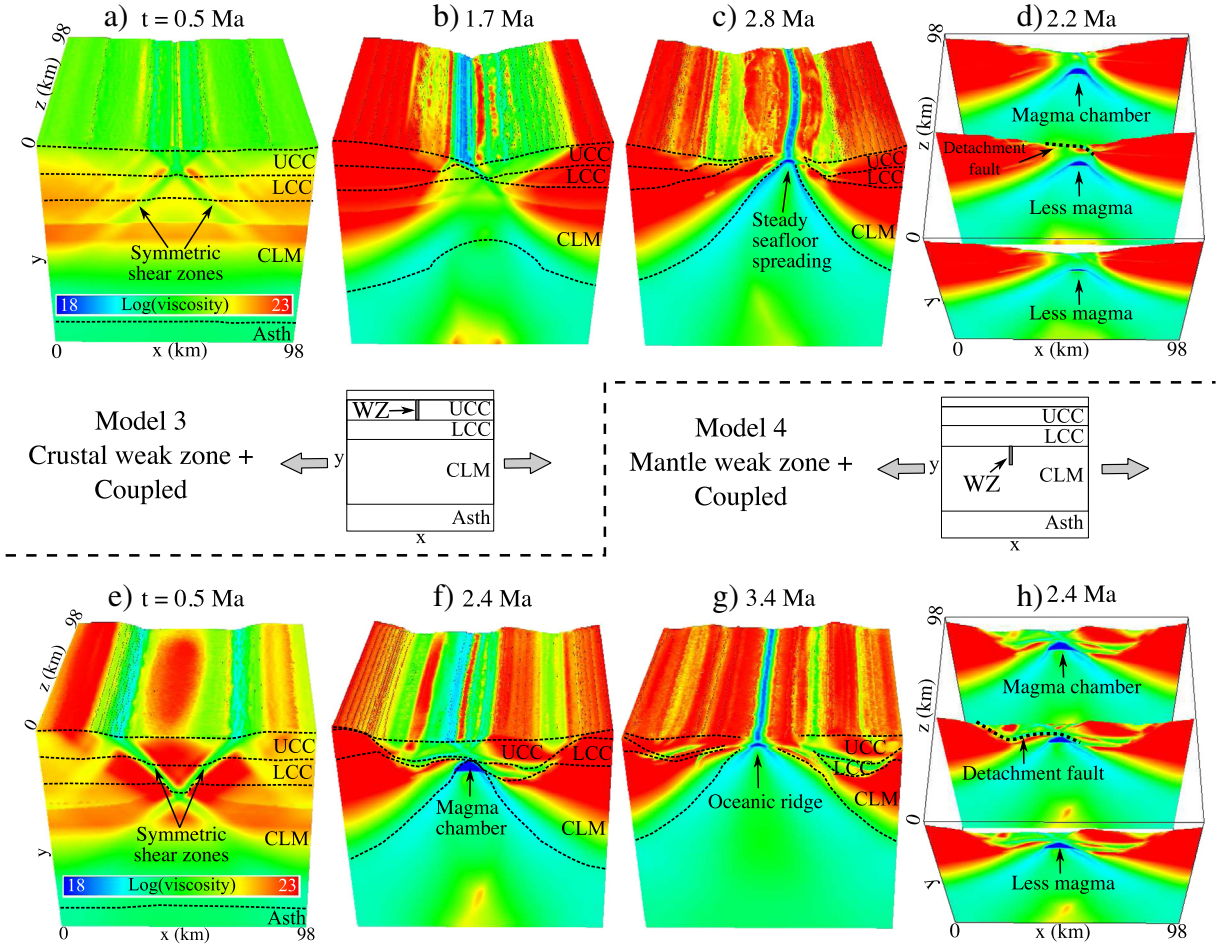

Fig. 3. Model evolution with the lithospheric coupled rheology. The 2D-like setups with crustal weak zone (a–d) and mantle weak zone (e–h) are used. High angle normal faults have been rotated to low angle detachment faults. WZ — weak zone, UCC — upper continental crust, LCC — lower continental crust, CLM — continental lithospheric mantle, and Asth — asthenosphere. Dashed lines show the interfaces between different rock layers.

average thickness of ~3.3 km of the oceanic crust for a 30 km/Ma full spreading rate.

3.2. 3D-like model setup

3.2.1. Decoupled rheology (DCP)

The 3D-like model setups (Fig. 1d) are used in this section. Instead of extending throughout the entire model box, the crustal or mantle weak zone has a length of 24.5 km along z-direction (perpendicular to extension). Dynamic evolution of the models with the decoupled rheology and a mantle weak zone is shown in Fig. 5. Model 5 has a weak zone located on one side of the model box (Fig. 5a), while Model 6 imposes a weak zone in the middle of the model box (Fig. 5e). Following the initial weak zone, continental rifts develop as a consequence of lithospheric thinning. Melt occurs first in the weak zone where the lithosphere thins the most (Fig. 5d and h). Lithospheric thinning has been further enhanced by the presence of melt. Seafloor spreading develops in a progressive propagation manner, and both models generate curved oceanic ridges (Figs. 5 and 6). The oceanic ridge is featured by asymmetric accretion involving active oceanic detachment faults which are established in the late continental rifting stage. Similar to the models using the 2D-like weak zones, the DCP models with the 3D-like weak zones generate larger magma chambers than the CP models (Fig. 6e). DCP models request a longer time to reach the steady state (Fig. 6e and f). Models with crustal weak zone are not shown, since the results are similar to that of Model 1.

3.2.2. Coupled rheology (CP)

The CP models (Model 7 which has a short crustal weak zone in the middle, and Model 8 which has a short mantle weak zone in the middle) generate relatively straight and symmetric oceanic ridges in a short time period (Fig. 6c–d). Modeling results are comparable to that using the 2D-like setups (Models 3 and 4). Molten asthenosphere occurs in a small area beneath the oceanic ridge, and a pair of narrow conjugate passive margin is formed. Along the passive margins, exhumed lithospheric mantle is observed, since high angle normal faults are rotated to low angle detachment faults. The location of the weak zone (either in the upper crust or in the uppermost mantle) influences the extend of strain localization (e.g. the intersection depth of the conjugate shear zones), but has no influence on the final continental breakup and incipient geometry of the oceanic ridge.

4. Discussions

4.1. Detachment fault formation

Continental and oceanic detachment faults are established in the CP and DCP models, respectively, and their dynamic evolutions are shown in Figs. 7 and 8. We identify the continental detachment fault based on three rules which are the common features of detachment faults (Lister et al., 1986; Lister and Davis, 1989; Hill et al., 1995; Weinberg et al., 2007). First, lower crust (or upper mantle) is exposed on the surface along the footwall of a detachment fault (e.g. Fig. 7a).

Please cite this article as: Liao, J., Gerya, T., From continental rifting to seafloor spreading: Insight from 3D thermo-mechanical modeling, Gondwana Research (2014), http://dx.doi.org/10.1016/j.gr.2014.11.004

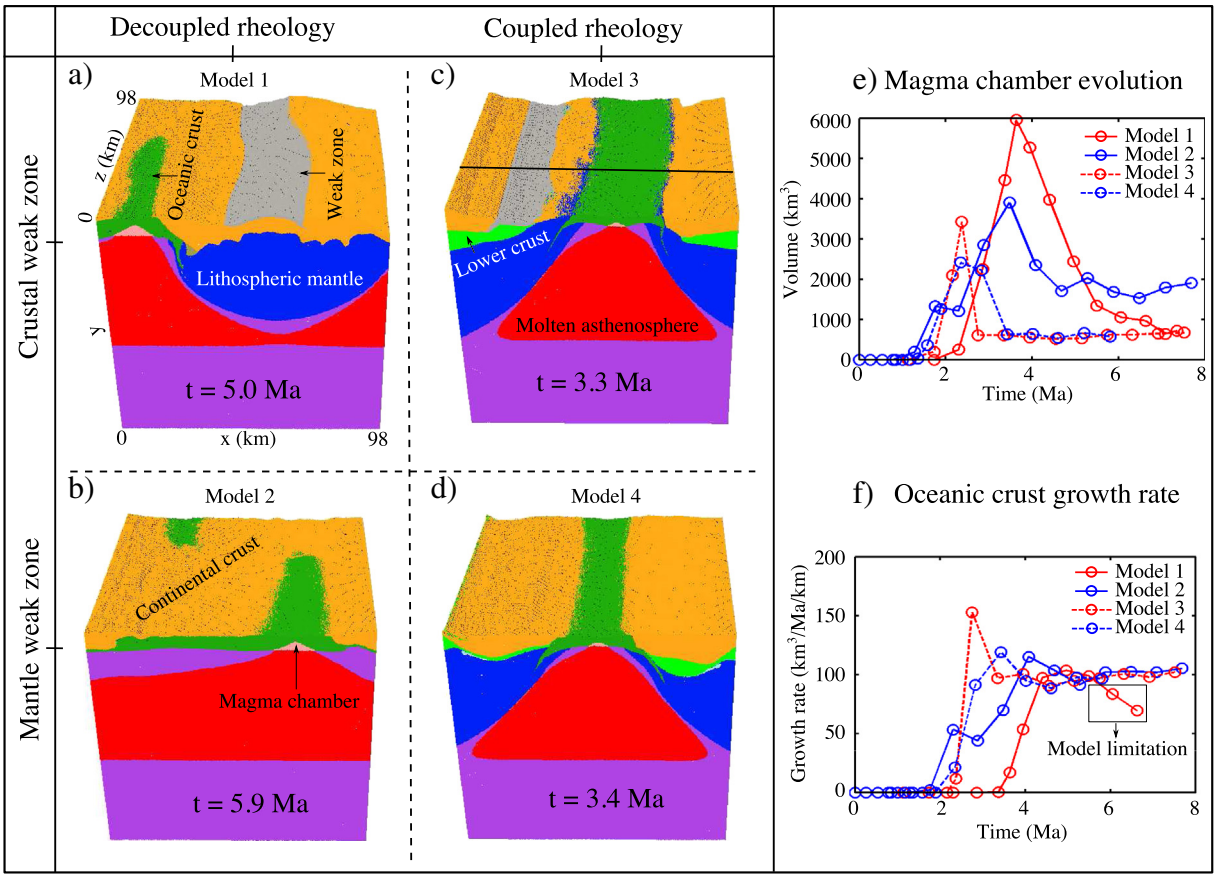

Fig. 4. Comparison of modeling results with the 2D-like setups. Lithospheric rheological coupling/decoupling and the weak zone location are varied in different models. Color shows composition (a–d), also see Fig. 1 for the color map. (e) Dynamic evolution of magma chamber volume and (f) growth rate of oceanic crust are compared. The black line in c shows the location of slices used in Figs. 7 and 9. Note that the decoupled rheology promotes asymmetric oceanic accretion, while the symmetric oceanic accretion is favored by coupled rheology.

Second, asthenosphere upwelling (or some magmatism) occurs beneath the footwall (e.g. Fig. 7a). Third, detachment faults have low viscosity (e.g. Fig. 7b) and high strain rate (e.g. Fig. 7c). The continental detachment faults are generated through fast rotation of the initial high angle normal faults (Fig. 7). Due to the localized lithospheric extension and thinning, one branch of the major conjugate faults is rotated to a low angle fault by the fast upwelling asthenosphere. The detachment faults that initiated and developed in the continental rifting stage are terminated in the late rifting–early spreading stage, by intensive magmatism (due to partial melting of upwelling asthenosphere), which cuts off the detachment faults and forms oceanic spreading (Lister et al., 1986; Ebinger and Casey, 2001; MacLeod et al., 2009).

Oceanic detachment faults are established during the late continental rifting–early seafloor spreading stage in the DCP models (Fig. 8). In this study, the term 'oceanic detachment fault' is used in a broad sense, for the low-angle large-offset normal faults (Gerya, 2010, 2013; Puthe and Gerya, 2014). Occurrence of oceanic core complexes (OCCs) is not specified in this broad sense terminology (Escartin et al., 2008). Thus, this definition differs from the more strict definition (Buck et al., 2005; MacLeod et al., 2009), according to which oceanic detachment faults should always be associated with OCCs. Amagmatic accretion (limited magma supply) is required for the formation of OCCs (Buck et al., 2005; MacLeod et al., 2009). In our models, however, oceanic accretion is featured by intensive magmatism, and newly formed oceanic crust fills spreading gap and inhibits the occurrence of OCCs. A test model with lower initial mantle temperature (Fig. 10b) produces large OCCs along the ridge axis since spreading is mainly accommodated by tectonic stretching.

In our models, oceanic detachment faults typically cause an asymmetric plate accretion (Gerya, 2010, 2013; Puthe and Gerya, 2014). Oceanic crust grows faster underneath the footwall of a detachment fault than underneath the hanging wall (e.g. Fig. 8a). The oceanic detachment fault shown in Fig. 8 originates from the conjugate normal faults. Following the location of the initial weak zone, two conjugate normal faults form along the walls of a wedge-like magma chamber in the late rifting stage (Fig. 8a and c). One branch of the conjugate normal faults evolves into a detachment fault (Fig. 8c), as strain weakening and shear heating amplify perturbations along the normal faults and break up the symmetry. On a map view, a 3D feature, i.e. the curved geometry of the oceanic detachment fault is revealed (t = 6.4 Ma in Fig. 8b). The 3D curved geometry (Escartin et al., 2008) of the oceanic detachment fault is formed due to the different initiation time of the detachment fault along z-direction (perpendicular to spreading direction). The oceanic detachment fault first initiates in the middle of the model, then propagates to the edges of the model. Asymmetric accretion of oceanic crust makes the detachment fault curved in a map, thus producing noticeable curvature of the oceanic ridge (Fig. 8b).

The formation of oceanic detachment faults is facilitated by magma supply in our models, indicating a dependence of oceanic detachment faults on magma supply. The results from Tucholke et al. (2008) show that a limited window of magmatism may be present, facilitating the formation of detachment faults. However, unlike the previous models in which newly formed oceanic crust is accreted to a hanging wall (Buck et al., 2005; Tucholke et al., 2008), newly formed oceanic crust in our models is accreted to the footwall (beneath the detachments) (Fig. 8a). This result is also shown in the studies by Puthe and Gerya (2014) and Gerya (2010, 2013). The total melt transported to the oceanic ridge from the mantle is the sum of the melt transported to the hanging wall and that delivered to the footwall (MacLeod et al., 2009). In the models by Buck et al. (2005) and Tucholke et al. (2008), melt

Please cite this article as: Liao, J., Gerya, T., From continental rifting to seafloor spreading: Insight from 3D thermo-mechanical modeling, Gondwana Research (2014), http://dx.doi.org/10.1016/j.gr.2014.11.004

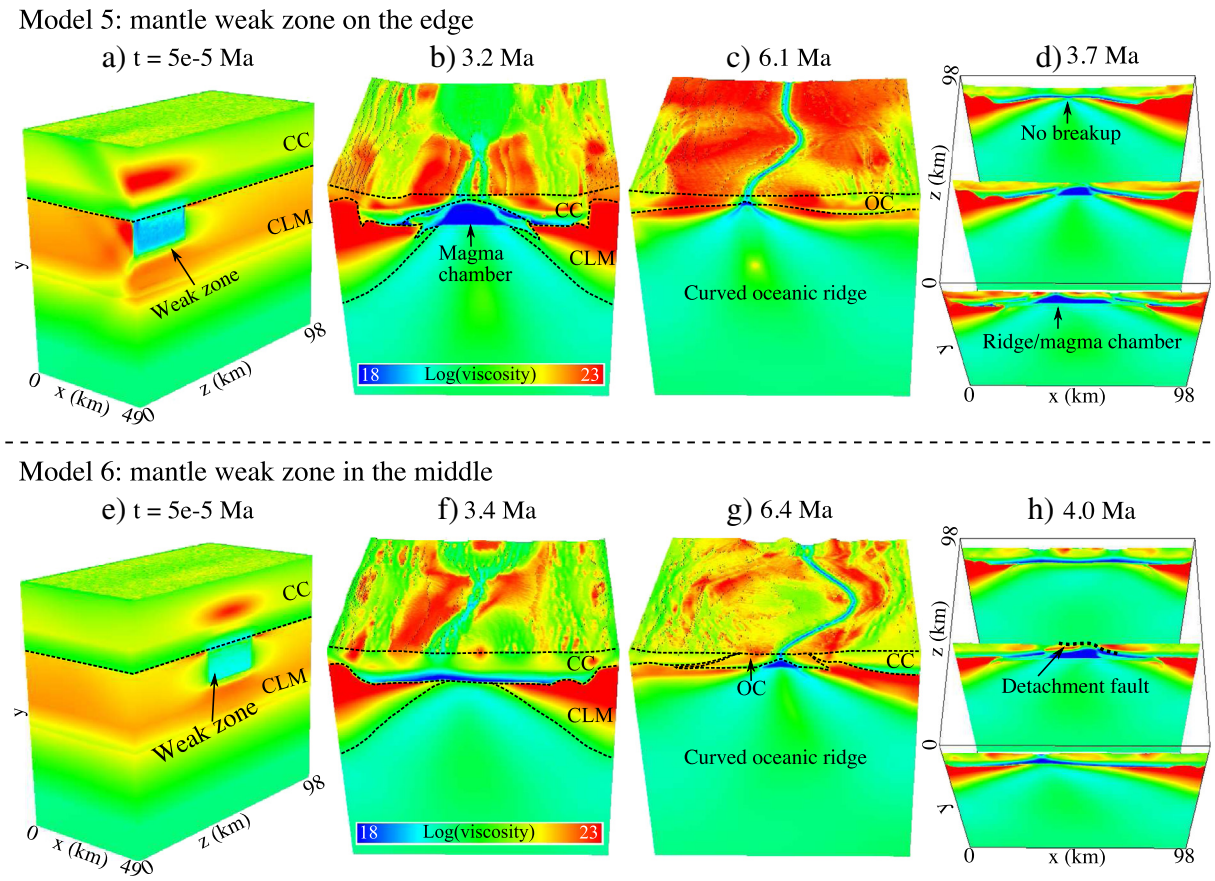

Fig. 5. Model evolution with the decoupled rheology using the 3D-like setups. A short mantle weak zone is located either on one side (a–d) or in the middle (d–h) of the model domain. Slices are shown at a certain time step for both models (d, h). CC — continental crust, CLM — continental lithospheric mantle, OC — oceanic crust.

is only transported to the hanging wall via dikes. However, this dike formation is not simulated in our models.

In the life cycle of oceanic core complexes demonstrated by MacLeod et al. (2009), oceanic detachment faults are terminated by magma that is delivered to the footwall. This feature is observed in our model results (Fig. 8). Magma cuts through the detachment faults (compare the snapshot at t = 6.4 Ma to the one at t = 5.8 Ma in Fig. 8c), changing the oceanic accretion pattern from asymmetric to symmetric. As a consequence, abandoned oceanic ridge is generated on the hanging wall (Fig. 8b–c, t = 6.4 Ma). The formation of the abandoned ridge is evidenced by the natural example on the Mid-Atlantic ridge at 5°S (Reston et al., 2002), where the extinct oceanic ridge and abandoned detachment faults are observed on the hanging wall (Fig. 8d). The reconstruction (Fig. 8d) based on the bathymetry data (matching the fault scarps on the two flanks of the active ridge) indicates that the two core complexes (numbered 1 and 2 in the Fig. 8d) were adjoined contemporaneously. Thus, the termination of an oceanic detachment fault may indicate the initiation of a new oceanic ridge.

4.2. Rheological coupling and inheritance of continental rifting

Our preliminary modeling results show that the decoupled rheology leads to asymmetric oceanic accretion through detachment faults, whereas the coupled rheology promotes symmetric oceanic accretion. One possible reason to this difference could be the strain localization pattern in the lithosphere (Fig. 9). In the DCP models, lithospheric extension is decoupled by the weak ductile lower crust, and strain localizes in both the crust and the lithospheric mantle (Fig. 9a and b). Decoupled rheology has been proposed as the reason for the earlier breakup of the mantle lithosphere compared to the crust (Huismans and Beaumont, 2011). This is consistent with our modeling results, such as in Model 1, where the lithospheric mantle breaks up much earlier than the crust. In the CP models, large conjugate shear zones form across the entire lithosphere and lead to fast continental breakup (Figs. 4 and 6). Fast upwelling of the asthenosphere (as well as partial melting) may suppress the development of oceanic detachment faults, and promotes symmetric oceanic accretion. Fast extension rate has a similar effect, resulting in a symmetric and straight oceanic ridge, since the lithosphere experiences rapid extension and thinning (Fig. 10d).

During continental rifting, heterogeneities are generated and amplified along the rift strike and influence seafloor spreading. Model 1 has a homogeneous long crustal weak zone extending through the entire model box along z-direction (Figs. 2 and 4a), however, extension is not uniformly distributed along the rift valley in the rifting stage, since the weakening effects (i.e. plastic strain weakening and shear heating) amplify initial small perturbations that are introduced by the randomly distributed markers. Moreover, the continental rift that formed in the early extension stage does not develop into a spreading ridge, but becomes abandoned. The spreading ridge establishes with an offset distance laterally from the abandoned rift. Continental breakup is dominated by the lithospheric mantle thinning which has a wavelength determined by the angle of the normal fault and the thickness of the brittle lithosphere (Fig. 10c). Abandoned continental rifts (i.e. rift jump) have been widely proposed to occur in nature (Wood, 1983; Armitage et al., 2010; Yamasaki and Gernigon, 2010). In the Benue Trough and Cameroon volcanic region as discussed by Wood (1983), the newly formed Cameroon volcanic line is offset from the abandoned Benue Trough, and it is featured by abundant volcanism but little faulting which suggests an active rifting pattern. Results of Model 1

Please cite this article as: Liao, J., Gerya, T., From continental rifting to seafloor spreading: Insight from 3D thermo-mechanical modeling, Gondwana Research (2014), http://dx.doi.org/10.1016/j.gr.2014.11.004

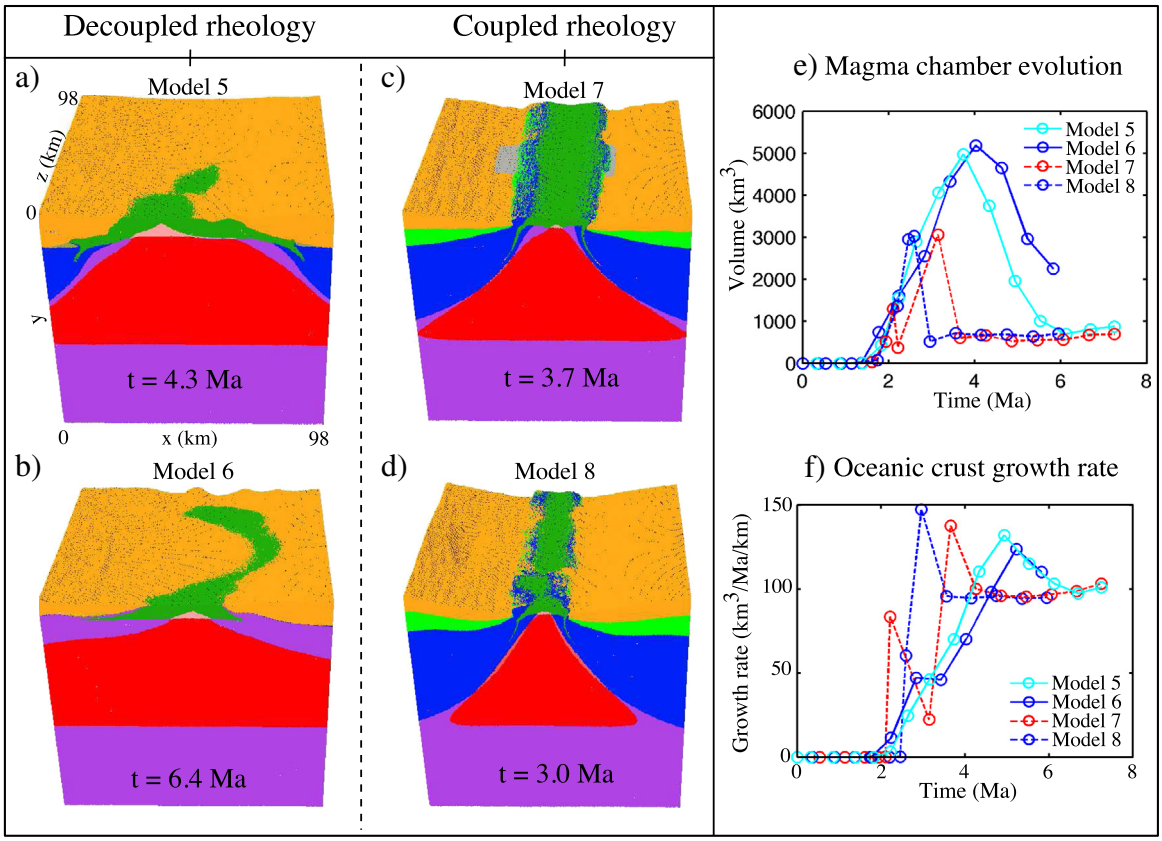

Fig. 6. Comparison of modeling results with the decoupled and coupled rheologies using the 3D-like setups. (a–d) Comparison of composition (see Figs. 1 and 4 for the color notation). (e) Dynamic evolution of magma chamber volume and (f) growth rate of oceanic crust are compared. Model 7 (c) has a crustal weak zone, and Model 8 (d) has a mantle weak zone, both of which are located in the middle of the model domain. Note that the decoupled rheology promotes asymmetric oceanic accretion, while the symmetric oceanic accretion is favored by the coupled rheology.

are consistent with these observations, as the mantle dominated thinning deforms the lithosphere in an active rifting pattern.

In Model 2, although a single straight and uniformly extended continental rift is generated in the early stage, two offset spreading ridges are established due to the formation of the opposite-dipping detachment faults (Figs. 2 and 4a). Development of the opposite-dipping detachments is crucial for transform fault formation (Gerya, 2010). However, it is difficult to predict which of the two branches of the conjugated normal faults becomes dominant. Large heterogeneities are generated along the rift strike during extension, which makes the formation of opposite-dipping detachment faults potentially possible. The two ridge segments in Model 2 propagate towards each other, but a transform fault is not formed. However, by slightly modifying the model setup (decreasing the height of the weak zone), a proto-

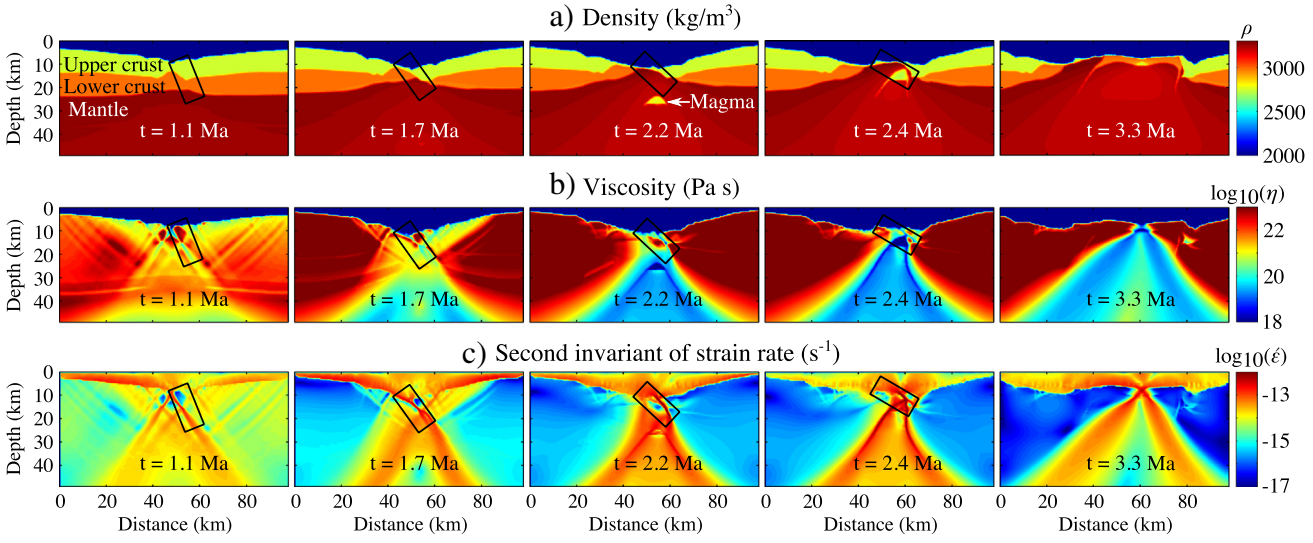

Fig. 7. Evolution of the continental detachment fault generated in Model 3. Location of the slices is shown in Fig. 4c by the black line (z = 38 km). (a) Density, (b) viscosity, and (c) second invariant of strain rate show the rotation of the high angle normal fault (highlighted by black rectangles).

Please cite this article as: Liao, J., Gerya, T., From continental rifting to seafloor spreading: Insight from 3D thermo-mechanical modeling, Gondwana Research (2014), http://dx.doi.org/10.1016/j.gr.2014.11.004

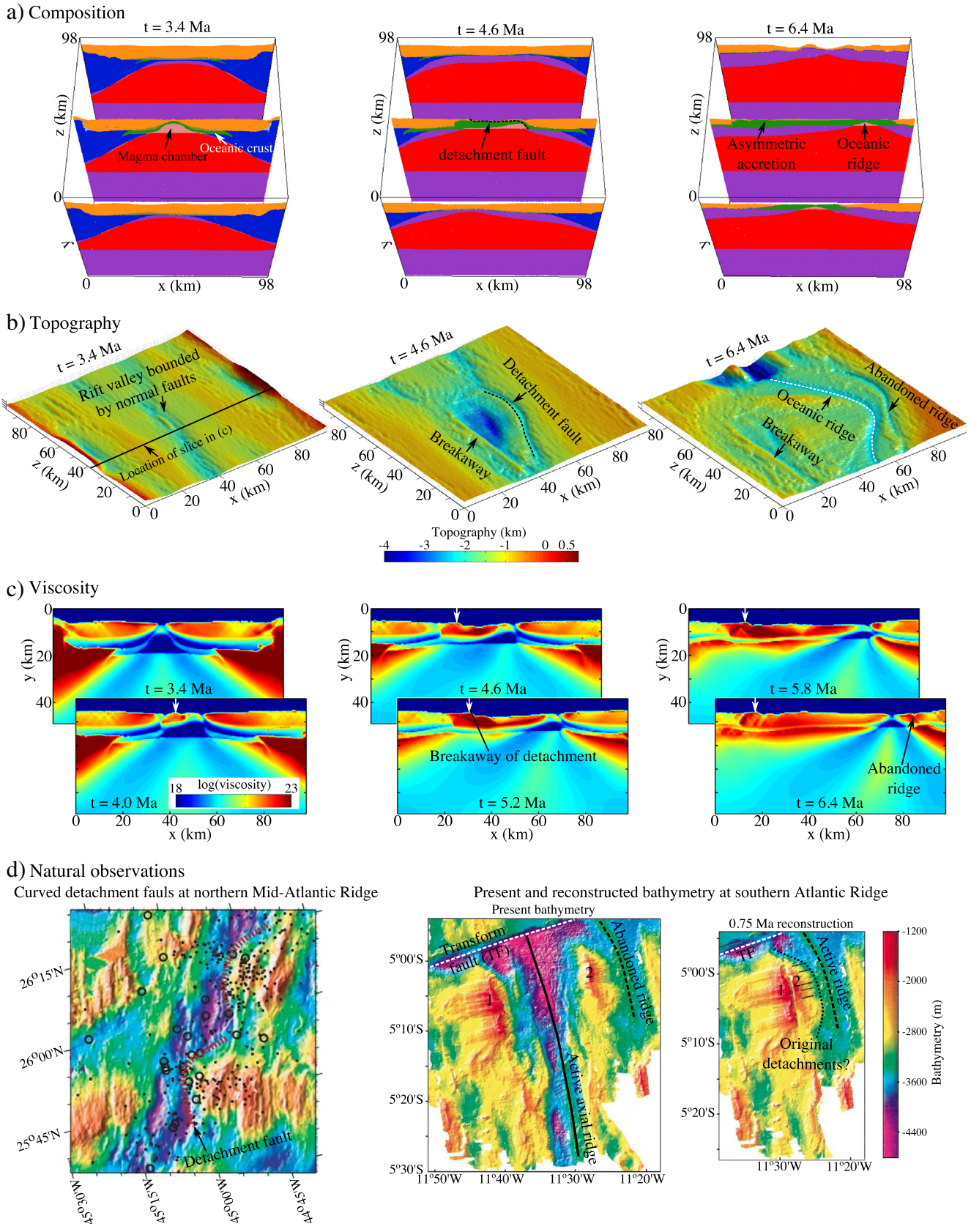

Fig. 8. Evolution of the detachment fault generated in Model 6 and comparison with natural examples. (a) Composition, (b) topography and (c) viscosity snapshots of the model results are shown for different times. The location of viscosity slices is shown in (b) by the black line (z = 38 km). White arrows in viscosity slices show the positions of detachment breakaway. (d) Natural examples of curved detachment faults at northern Mid-Atlantic Ridge (modified after Escartin et al. (2008)) and ridge abandonment at 5°S Atlantic ridge (modified after Reston et al. (2002)).

Please cite this article as: Liao, J., Gerya, T., From continental rifting to seafloor spreading: Insight from 3D thermo-mechanical modeling, Gondwana Research (2014), http://dx.doi.org/10.1016/j.gr.2014.11.004

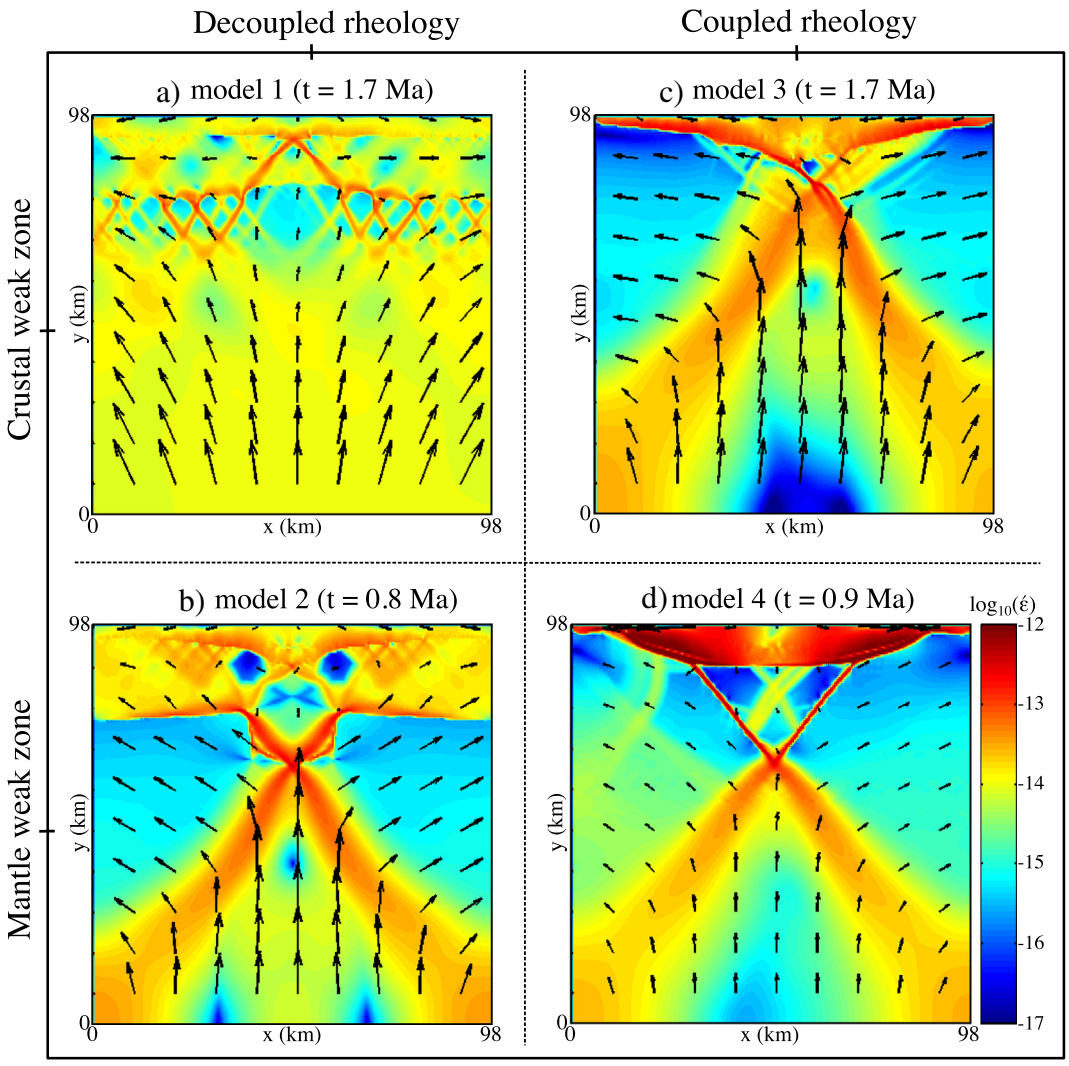

Fig. 9. Comparison of the second invariant of strain rate along xy slice at z = 38 km. See the location of the slice in Fig. 4c. Arrows show the velocity vectors (using velocity components of vx and vy).

transform fault is formed (Fig. 10a), which obliquely connects spreading ridges. Inheritance of continental rifting in seafloor spreading is also demonstrated by Model 5 (Figs. 5 and 6a), in which the spreading ridge propagates in a curved way. Numerous heterogeneities are generated during the rifting process, and subsequent continental breakup follows the weakest areas in the model.

4.3. Passive continental margins

In terms of magmatism, passive continental margins can be divided into two categories: magma-poor and magma-rich. Most (~90%) of the passive margins are magma-rich (Menzies et al., 2002; Reston, 2009). Magma-rich margins are featured by intensive magma activity (e.g. large igneous provinces, high-velocity lower crust, and seaward-dipping reflectors), which can occur before, during, or after continental breakup (Menzies et al., 2002). Magma-poor margins are featured by very limited magmatism (which mostly occurs in the late stage of continental rifting) and exhumed mantle peridotite in the ocean–continent transition zone (Reston, 2009). In our study, significant magmatism is occurring due to decompression melting of asthenosphere during rifting, and continental margins are featured as magma-rich. Magmatism is inhomogeneous along rifting strike (e.g. Figs. 2, 3 and 5), and the area with more magma production ruptures earlier. This is consistent with the previous study by Corti et al. (2003), which discussed that continental rifting occurs contemporaneously while break-up happens in a punctiform way.

The origin of magmatism along magma-rich margins is debated. Although plume formation is a prevailing mechanism since it can explain large igneous provinces (Menzies et al., 2002), mantle temperature anomalies (White and Mckenzie, 1989; Reston, 2009), mantle composition anomalies (Korenaga, 2004), and small-scale convection (Boutilier and Keen, 1999) are proposed as possible reasons. In our models, magmatism and oceanic crust thickness are mainly regulated by the mantle temperature (i.e. mantle temperature anomalies). With a higher initial mantle temperature, much thicker oceanic crust (>5 km) is generated in the models conducted by Puthe and Gerya (2014). Cool lithospheric mantle can significantly depress melting (Reston, 2009; Van Avendonk et al., 2009). A model with strongly lowered initial mantle temperature is shown in Fig. 10b, in which no partial melting is generated in the model, and exhumed lithospheric mantle and asthenosphere are found on the surface. Another possible reason for the intensive magma production in our models is the fast extension rate. Although a full extensional velocity of 3 cm/yr (corresponding to a bulk strain rate of $1.59 \times 10^{-15} s^{-1}$) is in a reasonable range for continental rifts (Buck, 1991),this rate is still above average since most continental rifts have an extension rate less than 1 cm/yr (Buck, 1991). Extension velocity has a significant effect on continental extension. Fast extension promotes earlier

Please cite this article as: Liao, J., Gerya, T., From continental rifting to seafloor spreading: Insight from 3D thermo-mechanical modeling, Gondwana Research (2014), http://dx.doi.org/10.1016/j.gr.2014.11.004

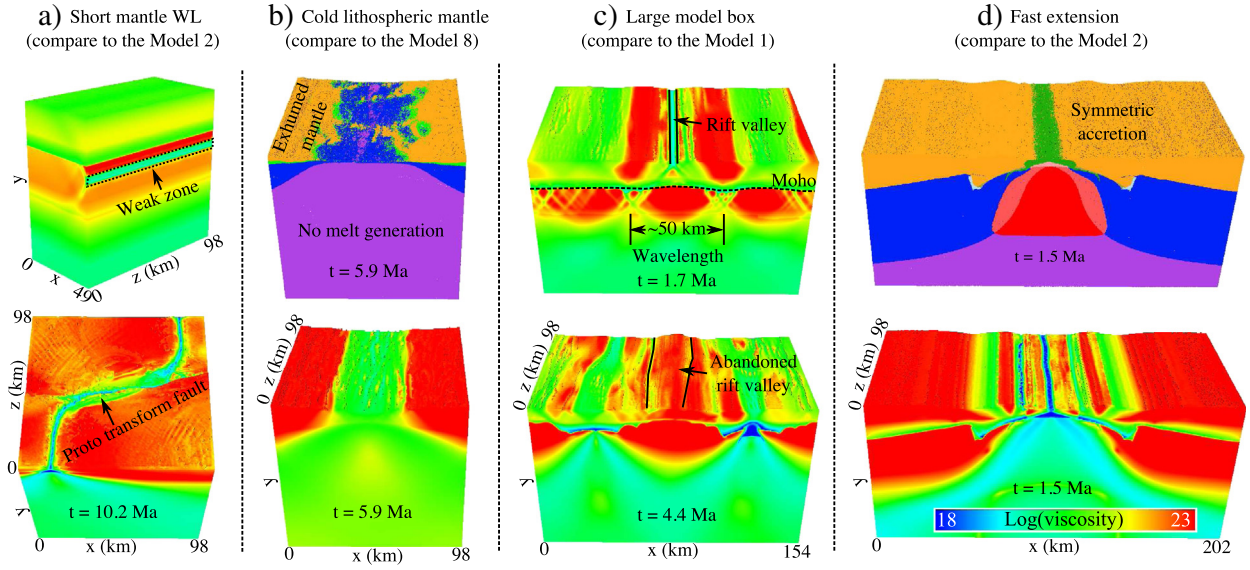

Fig. 10. Additional model runs. (a) Model with identical setup with respect to Model 2 except slightly decrease the weak zone height (dotted rectangle). (b) Model with cold lithosphere (i.e. initial temperature at the lithosphere–asthenosphere boundary is 1000 °C) based on Model 8. (c) Increase the model box size along the x-direction based on Model 1. Note that the results are highly similar to that of Model 1, in which offset rifting and spreading is generated. (d) Use large model box and fast extension rate (full rate 6.18 cm/yr) based on Model 2. See Figs. 1 and 4 for the composition notations.

strain localization, leads to narrow rifting and produces voluminuous magma, while slow extension favors widespread distributed deformation (Liao et al., 2013) (and supporting material). With slower extension, we would expect less magmatism.

In terms of rifting width, continental rifts generated in our models are narrow. Several parameters contribute to the fast strain localization along the prescribed weak zone during extension. The continental lithosphere used in our models is relatively young and warm (since lithospheric thickness is 80 km). The imposed extension rate is relatively fast for continental rifting as discussed above. These two factors may largely promote narrow rifting (e.g. Van Avendonk et al., 2009). Besides, the model dimension (parallel to extension) is quite small (~100 km) since we use high resolution. Increasing model dimensions to reduce boundary condition effects is therefore necessary for future studies.

5. Conclusion

Based on our modeling results, oceanic spreading has a strong dependence on continental rifting which is influenced by the initial rheological coupling/decoupling of the continental lithosphere (i.e. by the presence/absence of a strong lower crust). Rheological coupling/decoupling generates two types of incipient oceanic ridge development: (1) coupled lithospheric rheology promotes symmetric oceanic accretion, while (2) decoupled lithospheric rheology favors the formation of asymmetric oceanic accretion involving development of active detachment faults. In the models with coupled rheology, lithospheric scale shear zones are generated and lithosphere thins rapidly. The decoupled models extend in a depth-dependent way.

Two types of detachment faults develop in our numerical experiments. Continental detachment faults are found in the models with the coupled rheology and mainly develop during continental rifting stage. Intensive magmatism terminates these faults in the late rifting stage. Oceanic detachment faults form during oceanic spreading stage and cause asymmetric plate accretion. Magmatism can also terminate oceanic detachment faults, switching the mode of oceanic accretion from asymmetric to symmetric. Curved oceanic detachment faults can also be observed in our 3D models.

We also discussed the inheritance of continental rifting in oceanic spreading. Large heterogeneities are generated during continental rifting, and further influence oceanic ridge development. Modeled phenomena such as abandoned continental rift, opposite-dipping detachment faults and curved propagation of oceanic ridge are typical signatures of the continental rifting inheritance.

Acknowledgments

We thank D. May and F. Crameri for the discussion on 3-D visualization. Thorough and constructive reviews by G. Corti and J. van Hunen are much appreciated.

References

Afonso, J.C., Ranalli, G., 2004. Crustal and mantle strengths in continental lithosphere: is the jelly sandwich model obsolete? Tectonophysics 394, 221–232. http://dx.doi.org/10.1016/j.tecto.2004.08.006.

Allken, V., Huismans, R.S., 2012. Factors controlling the mode of rift interaction in brittle-ductile coupled systems: A 3d numerical study. Geochemistry, Geophysics, Geosystems 13, 1–18. http://dx.doi.org/10.1029/2012GC004077.

Allken, V., Huismans, R.S., Thieulot, C., 2011. Three-dimensional numerical modeling of upper crustal extensional system. Journal of Geophysical Research 116, 1–15. http://dx.doi.org/10.1029/2011JB008319.

Armitage, J.J., Collier, J.S., Minshull, T.A., 2010. The importance of rift history for volcanic margin formation. Nature 465, 913–917. http://dx.doi.org/10.1038/nature09063.

Bittner, D., Schmeling, H., 1995. Numerical modelling of melting processes and induced diapirism in the lower crust. Geophysical Journal International 123, 59–70.

Boutilier, R.R., Keen, C.E., 1999. Small-scale convection and divergent plate boundaries. Journal of Geophysical Research 104, 7389–7403.

Brace, W.F., Kohlstedt, D.L., 1980. Limits on lithospheric stress imposed by laboratory experiment. Journal of Geophysical Research 85, 6248–6252.

Brune, S., 2014. Evolution of stress and fault patterns in oblique rift systems: 3-D numerical lithospheric-scale experiments from rift to breakup. Geochemistry, Geophysics, Geosystems 15, 3392–3415. http://dx.doi.org/10.1002/2014GC005446.

Brune, S., Autin, J.a., 2013. The rift to break-up evolution of the Gulf of Aden: Insights from 3d numerical lithospheric-scale modelling. Tectonophysics 607, 65–79. http://dx.doi.org/10.1016/j.tecto.2013.06.029.

Brune, S., Popov, A.A., Sobolev, S.V., 2012. Modeling suggests that oblique extension facilitates rifting and continental break-up. Journal of Geophysical Research 117, 1–16. http://dx.doi.org/10.1029/2011JB008860.

Buck, W.R., 1991. Models of continental lithospheric extension. Journal of Geophysical Research 96, 20161–20178.

Buck, W.R., 2006. The role of magma in the development of the Afro-Arabian rift system. Geological Society, London, Special Publications 259, 43–54. http://dx.doi.org/10.1144/GSL.SP.2006.259.01.05.

Buck, W.R., Lavier, L.L., Poliakov, A.N.B., 1999. How to make a rift wide. Philosophical Transactions of the Royal Society A 357, 671–693. http://dx.doi.org/10.1098/rsta.1999.0348.

Buck, W.R., Lavier, L.L., Pollakov, A.N.B., 2005. Models of faulting at mid-ocean ridges. Nature 434, 719–723. http://dx.doi.org/10.1038/nature03358.

Please cite this article as: Liao, J., Gerya, T., From continental rifting to seafloor spreading: Insight from 3D thermo-mechanical modeling, Gondwana Research (2014), http://dx.doi.org/10.1016/j.gr.2014.11.004

Burgmann, R., Dresen, G., 2008. Rheology of the lower crust and upper mantle: evidence from rock mechanics, geodesy, and field observations. Annual Review of Earth and Planetary Sciences 36, 531–567. http://dx.doi.org/10.1146/annurev.earth.36.031207.124326.

Burov, E.B., 2010. The equivalent elastic thickness (te), seismicity and the long-term rheology of continental lithosphere: Time to burn-out "crème brûlée"? Insights from large-scale geodynamic modeling. Tectonophysics 484, 4–26. http://dx.doi.org/10.1016/j.tecto.2009.06.013.

Burov, E.B., Watts, A.B., 2006. The long-term strength of continental lithosphere: "jelly sandwich" or "crème brûlée"? GSA Today 16.

Byerlee, J., 1978. Friction of rocks. Pure and Applied Geophysics 116, 615–626.

Choi, E., Lavier, L., Gurnis, M., 2008. Thermomechanics of mid-ocean ridge segmentation. Physics of the Earth and Planetary Interiors 171, 374–386. http://dx.doi.org/10.1016/j.pepi.2008.08.010.

Clauser, C., Huenges, E., 1995. Thermal conductivity of rocks, minerals. In: Ahrens, T.J. (Ed.), Rock Physics and Phase Relations. American Geophysical Union, Washington, DC, pp. 105–126.

Corti, G., 2008. Control of rift obliquity on the evolution and segmentation of the main Ethiopian rift. Nature Geoscience 1, 258–262. http://dx.doi.org/10.1038/ngeo160.

Corti, G., 2009. Continental rift evolution: From rift initiation to incipient break-up in the Main Ethiopian Rift, East Africa. Earth-Science Reviews 96, 1–53. http://dx.doi.org/10.1016/j.earscirev.2009.06.005.

Corti, G., 2012. Evolution and characteristics of continental rifting: Analog modeling-inspired view and comparison with examples from the East African Rift System. Tectonophysics 522–523, 1–33. http://dx.doi.org/10.1016/j.tecto.2011.06.010.

Corti, G., Van Wijk, J., Bonini, M., Sokoutis, D., Cloetingh, S., Innocenti, F., Manetti, P., 2003. Transition from continental break-up to punctiform seafloor spreading: How fast, symmetric and magmatic. Geophysical Research Letters 30. http://dx.doi.org/10.1029/2003GL017374.

Corti, G., Van Wijk, J.W., Cloetingh, S., Morley, K., 2007. Tectonic inheritance and continental rift architecture: Numerical and analogue models of the east African rift system. Tectonics 26, 1–13. http://dx.doi.org/10.1029/2006TC002086.

Crameri, F., Schmeling, H., Golabek, G.J., Duretz, T., Orendt, R., Buiter, S.J.H., May, D.A., Kaus, B.J.P., Gerya, T.V., Tackley, P.J., 2012. A comparison of numerical surface topography calculations in geodynamic modelling: an evaluation of the 'sticky air' method. Geophysical Journal International 189, 38–54. http://dx.doi.org/10.1111/j.1365-246X.2012.05388.x.

d'Acremont, E., Leroy, S., Maia, M., Gente, P., Autin, J., 2010. Volcanism, jump and propagation on the Sheba ridge, eastern Gulf of Aden: segmentation evolution and implications for oceanic accretion processes. Geophysical Journal International 180, 535–551. http://dx.doi.org/10.1111/j.1365-246X.2009.04448.x.

Dick, H.J.B., Lin, J., Schouten, H., 2003. An ultraslow-spreading class of ocean ridge. Nature 426, 405–412.

Dunbar, J.A., Sawyer, D.S., 1988. Continental rifting at pre-existing lithospheric weaknesses. Nature 333, 450–452.

Ebinger, C.J., Casey, M., 2001. Continental breakup in magmatic provinces: An Ethiopian example. Geology 29, 527–530.

Engen, O., Eldholm, O., Bungum, H., 2003. The arctic plate boundary. Journal of Geophysical Research 108, 2075–2092. http://dx.doi.org/10.1029/2002JB001809.

Escartin, J., Smith, D.K., Cann, J., Schouten, H., Langmuir, C.H., Escrig, S., 2008. Central role of detachment faults in accretion of slow-spreading oceanic lithosphere. Nature 455, 792–794. http://dx.doi.org/10.1038/nature07333.

Franke, D., Hinz, K., Oncken, O., 2001. The Laptev Sea Rift. Marine and Petroleum Geology 18, 1083–1127.

Gerya, T., 2010. Dynamics instability produces transform faults at mid-ocean ridges. Science 329, 1047–1050. http://dx.doi.org/10.1126/science.1191349.

Gerya, T., 2012. Origin and models of oceanic transform faults. Tectonophysics 522–523, 34–54. http://dx.doi.org/10.1016/j.tecto.2011.07.006.

Gerya, T.V., 2013. Three-dimensional thermomechanical modeling of oceanic spreading initiation and evolution. Physics of the Earth and Planetary Interiors 214, 35–52. http://dx.doi.org/10.1016/j.pepi.2012.10.007.

Gerya, T.V., Yuen, D.A., 2003. Characteristics-based marker-in-cell method with conservative finite-differences schemes for modeling geological flows with strongly variable transport properties. Physics of the Earth and Planetary Interiors 140, 293–318. http://dx.doi.org/10.1016/j.pepi.2003.09.006.

Gerya, T.V., Yuen, D.A., 2007. Robust characteristics method for modelling multiphase visco-elasto-plastic thermo-mechanical problems. Physics of the Earth and Planetary Interiors 163, 83–105. http://dx.doi.org/10.1016/j.pepi.2007.04.015.

Gregg, P.M., Behn, M.D., Lin, J., Grove, T.L., 2009. Melt generation, crystallization, and extraction beneath segmented oceanic transform faults. Journal of Geophysical Research 114, 1–16. http://dx.doi.org/10.1029/2008JB006100.

Hess, P.C., 1989. Origin of Igneous Rocks. Harvard University Press, London, UK.

Hill, E.J., Baldwin, S.L., Lister, G.S., 1995. Magmatism as an essential driving force for formation of active metamorphic core complexes in eastern Papua New Guinea. Journal of Geophysical Research 100, 10441–10451. http://dx.doi.org/10.1029/94JB03329.

Huismans, R.S., Beaumont, C., 2003. Symmetric and asymmetric lithospheric extension: Relative effects of frictional-plastic and viscous strain softening. Journal of Geophysical Research 108, 1–13. http://dx.doi.org/10.1029/2002JB002026.

Huismans, R., Beaumont, C., 2011. Depth-dependent extension, two-stage breakup and cratonic underplating at rifted margins. Nature 473, 74–79.

Jackson, J., 2002. Strength of the continental lithosphere: Time to abandon the jelly sandwich? GSA Today 12, 4–10. http://dx.doi.org/10.1130/1052-5173(2002)012<0004:SoTCIT>2.0.Co;2.

Johannes, W., 1985. The significance of experimental studies for the formation of migmatites. In: Ashworth, J. (Ed.), Migmatites. Blackie, Glasgow, UK, pp. 36–85.

Karato, S., 1992. On the Lehmann discontinuity. Geophysical Research Letters 19, 2255–2258.

Karato, S., 2010. Rheology of the deep upper mantle its implications for the preservation of the continental roots: A review. Tectonophysics 481, 82–98. http://dx.doi.org/10.1016/j.tecto.2009.04.011.

Katayama, I., Karato, S., 2008. Low-temperature, high-stress deformation of olivine under water-saturated conditions. Physics of the Earth and Planetary Interiors 168, 125–133. http://dx.doi.org/10.1016/j.pepi.2008.05.019.

Katz, R.F., Spiegelman, M., Langmuir, C.H., 2003. A new parameterization of hydrous mantle melting. Geochemistry, Geophysics, Geosystems 4, 1–19. http://dx.doi.org/10.1029/2002GC000433.

Keranen, K., Klemperer, S.L., 2008. Discontinuous and diachronous evolution of the Main Ethiopian Rift: Implications for development of continental rifts. Earth and Planetary Science Letters 265, 96–111.

Korenaga, J., 2004. Mantle mixing and continental breakup magmatism. Earth and Planetary Science Letters 218, 463–473. http://dx.doi.org/10.1016/S0012-821X(03)00674-5.

Leroy, S., Lucazeau, F., d'Acremont, E., Watremez, L., Autin, J., Rouzo, S., Bellahsen, N., Tiberi, C., Ebinger, C., Beslier, M., Perrot, J., Razin, P., Rolandone, F., Sloan, H., Stuart, G., Lazki, A.A., Al-Toubi, K., Bache, F., Bonneville, A., Goutorbe, B., Huchon, P., Unternehr, P., Khanbari, K., 2010. Contrasted styles of rifting in the eastern Gulf of Aden: A combined wide-angle, multichannel seismic, and heat flow survey. Geochemistry, Geophysics, Geosystems 11, 1–14. http://dx.doi.org/10.1029/2009GC002963.

Liao, J., Gerya, T., 2014. Influence of lithospheric mantle stratification on craton extension: Insight from two-dimensional thermo-mechanical modeling. Tectonophysics http://dx.doi.org/10.1016/j.tecto.2014.01.020.

Liao, J., Gerya, T., Wang, Q., 2013. Layered structure of the lithospheric mantle changes dynamics of craton extension. Geophysical Research Letters 40, 1–6. http://dx.doi.org/10.1002/2013GL058081.

Ligi, M., Bonatti, E., Bortoluzzi, G., Cipriani, A., Cocchi, L., Tontini, F.C., 2012. Birth of an ocean in the Red Sea: Initial pangs. Geochemistry, Geophysics, Geosystems 13, 1–29. http://dx.doi.org/10.1029/2012GC004155.

Lister, G.S., Davis, G.A., 1989. The origin of metamorphic core complexes and detachment faults formed during tertiary continental extension in the northern Colorado river region, U.S.A. Journal of Structural Geology 11, 65–94.

Lister, G.S., Etheridge, M.A., Symonds, P.A., 1986. Detachment faulting and the evolution of passive continental margins. Geology 14, 246–250. http://dx.doi.org/10.1130/0091-7613(1986)14<246:DFATEO>2.0.CO;2.

MacLeod, C.J., Searle, R.C., Murton, B.J., Casey, J.F., Mallows, C., Unsworth, S.C., Achenbach, K.L., Harris, M., 2009. Life cycle of oceanic core complexes. Earth and Planetary Science Letters 287, 333–344. http://dx.doi.org/10.1016/j.epsl.2009.08.016.

Maggi, A., Jackson, J.A., Priestley, K., Baker, C., 2000. A re-assessment of focal depth distributions in southern Iran, the Tien Shan and northern India: do earthquakes really occur in the continental mantle? Geophysical Journal International 143, 629–661.

Menzies, M.A., Klemperer, S.L., Ebinger, C.J., Baker, J., 2002. Characteristics of volcanic rifted margins. In: Menzies, M.A., Klemperer, S.L., Ebinger, C.J., Baker, J. (Eds.), Volcanic Rifted Margins. Geological Society of America Special Paper, Boulder, Colorado vol. 362.

Nielsen, T.K., Hopper, J.R., 2004. From rift to drift: Mantle melting during continental breakup. Geochemistry, Geophysics, Geosystems 5, 1–24. http://dx.doi.org/10.1029/2003GC000662.

Nyblade, A.A., Brazier, R.A., 2002. Precambrian lithospheric controls on the development of the east African rift system. Geology 30, 755–758.

Petit, C., Deverchere, J., 2006. Structure and evolution of the Baikal rift: A synthesis. Geochemistry, Geophysics, Geosystems 7, 1–26. http://dx.doi.org/10.1029/2006GC001265.

Poli, S., Schmidt, M.W., 2002. Petrology of subducted slabs. Annual Review of Earth and Planetary Sciences 30, 207–235. http://dx.doi.org/10.1146/annurev.earth.30.091201.140550.

Puthe, C., Gerya, T., 2014. Dependence of mid-ocean ridge morphology on spreading rate in numerical 3-D models. Gondwana Research 25, 270–283. http://dx.doi.org/10.1016/j.gr.2013.04.005.

Ranalli, G., 1995. Rheology of the Earth. Chapman & Hall, London, UK.

Reston, T.J., 2009. The structure, evolution and symmetry of the magma-poor rifted margins of the North and Central Atlantic: A synthesis. Tectonophysics 468, 6–27. http://dx.doi.org/10.1016/j.tecto.2008.09.002.

Reston, T.J., Weinrebe, W., Grevemeyer, I., Flueh, E.R., Mitchell, N.C., Kirstein, L., Kopp, C., Kopp, H., Participant of Meteror 47/2, 2002. A rifted inside corner massif on the mid-Atlantic ridge at 5°S. Earth and Planetary Science Letters 200, 255–269.

Schmeling, H., Babeyko, A.Y., Enns, A., Faccenna, C., 2008. A benchmark comparison of spontaneous subduction models—towards a free surface. Physics of the Earth and Planetary Interiors 171, 198–223. http://dx.doi.org/10.1016/j.pepi.2008.06.028.

Schmidt, M.W., Poli, S., 1998. Experimentally based water budgets for dehydrating slabs and consequences for arc magma generation. Earth and Planetary Science Letters 163, 361–379.

Smith, D.K., Cann, J.R., Escartin, J., 2006. Widespread active detachment faulting and core complex formation near 13° N on the Mid-Atlantic Ridge. Nature 442. http://dx.doi.org/10.1038/nature04950.

Sokoutis, D., Corti, G., Bonini, M., Brun, J.P., Cloetingh, S., Mauduit, T., Manetti, P., 2007. Modeling the extension of heterogeneous hot lithosphere. Tectonophysics 444, 63–79. http://dx.doi.org/10.1016/j.tecto.2007.08.012.

Taylor, B., Goodliffe, A.M., Martinez, F., 1999. How continents break up: Insights from Papua New Guinea. Journal of Geophysical Research 104, 7497–7512.

Taylor, B., Goodliffe, A.M., Martinez, F., 2009. Initiation of transform faults at rifted continental margins. Comptes Rendus Geoscience 341.

Please cite this article as: Liao, J., Gerya, T., From continental rifting to seafloor spreading: Insight from 3D thermo-mechanical modeling, Gondwana Research (2014), http://dx.doi.org/10.1016/j.gr.2014.11.004

Tucholke, B.E., Behn, M.D., Buck, W.R., Lin, J., 2008. Role of melt supply in oceanic detachment faulting and formation of megamullions. Geology 36, 455–458. http://dx.doi.org/10.1130/G24639A.1.

Turcotte, D.L., Schubert, G., 2002. Geodynamics. Cambridge University Press, Cambridge, UK.

Van Avendonk, H.J.A., Lavier, L.L., Shillington, D.J., Manatschal, G., 2009. Extension of continental crust at the margin of the eastern Grand Banks, Newfoundland. Tectonophysics 468, 131–148. http://dx.doi.org/10.1016/j.tecto.2008.05.030.

Van Wijk, J., 2005. Role of weak zone orientation in continental lithosphere extension. Geophysical Research Letters 32, 1–4. http://dx.doi.org/10.1029/2004GL022192.

Van Wijk, J.W., Blackman, D.K., 2005. Dynamics of continental rift propagation: the end-member modes. Earth and Planetary Science Letters 229, 247–258.

Wanless, V.D., Shaw, A.M., 2012. Lower crustal crystallization and melt evolution at mid-ocean ridges. Nature Geoscience 5, 651–655. http://dx.doi.org/10.1038/NGEO1552.

Weinberg, R.F., Regenauer-Lieb, K., Rosenbaum, G., 2007. Mantle detachment faults and the breakup of cold continental lithosphere. Geology 35, 1035–1038. http://dx.doi.org/10.1130/G23918A.1.

White, R., Mckenzie, D., 1989. Magmatism at rift zones: The generation of volcanic continental margins and flood basalts. Journal of Geophysical Research 94, 7685–7729.

Wilson, J.T., 1965. A new class of faults and their bearing on continental drift. Nature 207, 343–347.

Wilson, J.T., 1966. Did the Atlantic close and then re-open? Nature 211, 676–681.

Wood, C.A., 1983. Continental rift jumps. Tectonophysics 94, 529–540.

Yamasaki, T., Gernigon, L., 2010. Redistribution of the lithosphere deformation by the emplacement of underplated mafic bodies: implications for microcontinent formation. Journal of the Geological Society 167, 961–971. http://dx.doi.org/10.1144/0016-76492010-027.

Please cite this article as: Liao, J., Gerya, T., From continental rifting to seafloor spreading: Insight from 3D thermo-mechanical modeling, Gondwana Research (2014), http://dx.doi.org/10.1016/j.gr.2014.11.004